New Journal of Physics
The open access journal at the forefront of physics

Deutsche Physikalische Gesellschaft DPG
IOP Institute of Physics

Published in partnership with: Deutsche Physikalische Gesellschaft and the Institute of Physics

OPEN ACCESS

RECEIVED
10 May 2018

REVISED
26 July 2018

ACCEPTED FOR PUBLICATION
27 September 2018

PUBLISHED
15 October 2018

PAPER

The effective increase in atomic scale disorder by doping and superconductivity in $Ca_3Rh_4Sn_{13}$

A Ślebarski[1,2], P Zajdel[1], M Fijałkowski[1], M M Maśka[1], P Witas[1], J Goraus[1], Y Fang[3,4], D C Arnold[5] and M B Maple[3]

[1] Institute of Physics, University of Silesia in Katowice, ul. 75 Pułku Piechoty 1A, 41-500 Chorzów, Poland
[2] Centre for Advanced Materials and Smart Structures, Polish Academy of Sciences, Okólna 2, 50-950 Wrocław, Poland
[3] Department of Physics, University of California, San Diego, La Jolla, CA 92093, United States of America
[4] Materials Science and Engineering Program, University of California, San Diego, La Jolla, CA 92093, United States of America
[5] School of Physical Sciences, University of Kent, Canterbury, Kent CT2 7NH, United Kingdom

E-mail: andrzej.slebarski@us.edu.pl

Keywords: superconductivity, atomic disorder, electronic band structure, thermodynamic and transport properties

Abstract

A comprehensive study of the electronic structure, thermodynamic and electrical transport properties reveals the existence of inhomogeneous superconductivity due to structural disorder in $Ca_3Rh_4Sn_{13}$ doped with La ($Ca_{3-x}La_xRh_4Sn_{13}$) or Ce ($Ca_{3-x}Ce_xRh_4Sn_{13}$) with superconducting critical temperatures $T_c^\star$ higher than those (T_c) observed in the parent compounds. The $T-x$ diagrams and the entropy $S(x)_T$ isotherms document well the relation between the degree of atomic disorder and separation of the *high-temperature* $T_c^\star$ and T_c-bulk phases. In these dirty superconductors, with the mean free path much smaller than the coherence length, the Werthamer–Helfand–Hohenber theoretical model does not fit well the $H_{c2}(T)$ data. We demonstrate that this discrepancy can result from the presence of strong inhomogeneity or from two-band superconductivity in these systems. Both the approaches very well describe the $H-T$ dependencies, but the present results as well as our previous studies give stronger arguments for the scenario based on the presence of nanoscopic inhomogeneity of the superconducting state. A comparative study of La-doped and Ce-doped $Ca_3Rh_4Sn_{13}$ showed that in the disordered $Ca_{3-x}Ce_xRh_4Sn_{13}$ alloys the presence of spin-glass effects is the cause of the additional increase of $T_c^\star$ in respect to the critical temperatures of disordered $Ca_{3-x}La_xRh_4Sn_{13}$. We also revisited the nature of structural phase transition at $T^\star \sim 130 \div 170$ K and documented that there might be another precursor transition at higher temperatures. Raman spectroscopy and thermodynamic properties suggest that this structural transition may be associated with a CDW-type instability.

1. Introduction

The family of $R_3M_4Sn_{13}$ compounds, where R is an alkali metal or rare earth and M is a transition metal (Ir, Rh, Ru, or Co), was first synthesized by Remeika *et al* [1]. Recently, there has been a resurgence of interest among the condensed matter community due to unusual properties of these materials, characterized by strong electron correlation effects [2], structural phase transitions associated with the Fermi surface reconstruction [3–6], and superconductivity [7–9]. $Ca_3Rh_4Sn_{13}$, a member of this skutterudite-related family is a good model material to study the various low-temperature and structural properties. $Ca_3Rh_4Sn_{13}$ adopts the $Pm\bar{3}n$ cubic structure and has been found to be a BCS superconductor with a superconducting transition temperature T_c of about 8.4 K, which can be strongly reduced by antisite defects generated by different heat treatment [10, 11]. Similarly, an atomic disorder can occur as a result of doping. Recently, we documented experimentally, that the effect of nanoscale disorder generated by doping of the $Ca_3Rh_4Sn_{13}$ [12] and isostructural $La_3M_4Sn_{13}$ [13] superconductors leads to the appearance of an inhomogeneous superconducting state, characterized by the critical temperature $T_c^\star$ higher than T_c of the bulk phase. Similar interesting behavior has been observed in a

number of other strongly-correlated superconductors (see, e.g., [13–19]), particularly those close to a quantum critical point (QCP), where an increase of T_c was documented by nanoscale electronic disorder. In the critical regime, such a system is at the threshold of an instability, and even a weak perturbation, such as disorder can cause significant macroscopic effects. This is a reason for continuing our research of the atomic scale disorder and its impact on a novel phenomena in $Ca_3Rh_4Sn_{13}$ and similar materials. Moreover, for a series of $R_3M_4Sn_{13}$ it was claimed that the cubic crystallographic structure $Pm\bar{3}n$ is modulated below temperature $T^\star \sim 130$–170 K with a structural modulation indexed by a wave vector $\mathbf{q} = \left(\frac{1}{2}, \frac{1}{2}, 0\right)$ and its symmetry equivalents $\left(\frac{1}{2}, 0, \frac{1}{2}\right)$, $\left(0, \frac{1}{2}, \frac{1}{2}\right)$. In isostructural compound $Ca_3Ir_4Sn_{13}$, $T^\star$ has been reported much smaller ~40 K [3]. The structural second order-type transition at $T^\star$ converts the simple cubic high-temperature structure $Pm\bar{3}n$ into a body centered cubic structure $I4_132$ [20] with twice the lattice parameters due to the distortion of the $Sn1Sn2_{12}$ icosahedra related to a charge transfer from Sn2 toward Sn1 atoms[6]. The most possible scenario for the structural deformation of the La and Ce doped $Ca_3Rh_4Sn_{13}$ is a charge density wave (CDW) instability, which has been independently singled out by experimental [21] and theoretical [22, 23] investigations as a precursor for superconductivity. However, no signature of this anomaly associated with $T^\star$ was observed for undoped $Ca_3Rh_4Sn_{13}$. We documented, that Ca, when partially replaced by La ($Ca_{3-x}La_xRh_4Sn_{13}$) or Ce ($Ca_{3-x}Ce_xRh_4Sn_{13}$), which simulates a negative chemical pressure, revealed the existence of this structural transformation at the presence of T_c and $T_c^\star$ superconducting phases.

Recently, it was also shown that this phase transition remains second-order at $T = 0$, which leads to novel structural QCP [3, 8, 9]. In this manuscript, we discuss the impact of the magnetic correlations on the increase of T_c and $T_c^\star$ of the Ce-doped alloys with respect to superconducting temperatures of $Ca_{3-x}La_xRh_4Sn_{13}$. On the basis of electrical transport, thermodynamic properties, and band structure calculations we propose a phenomenological model, which qualitatively interprets the experimental data. Finally, we revisit the effect of structural instability at $T^\star$ and show that there might be another, precursor transition at higher temperatures.

2. Experimental details

The $Ca_3Rh_4Sn_{13}$, $La_3Rh_4Sn_{13}$ and $Ce_3Rh_4Sn_{13}$ polycrystalline samples were prepared by arc melting the constituent elements on a water cooled copper hearth in a high-purity argon atmosphere with an Al getter. The $Ca_{3-x}La_xRh_4Sn_{13}$ and $Ca_{3-x}Ce_xRh_4Sn_{13}$ alloys were then prepared by diluting the parent compounds with nominal compositions of La or Ce and Ca which were then annealed at 870 °C for 2 weeks. All samples were examined by x-ray diffraction (XRD) analysis and in the first approximation found to have a cubic structure (space group $Pm\bar{3}n$) [1].

Variable temperature powder XRD measurements were carried out on a single crystal diffractometer Rigaku (Oxford Diffraction) Supernova in a powder mode using Cu K_α microsource (50 kV, 0.80 mA). Small amounts of samples (<1 mg) were powdered before the experiments and glued to a tip of a glass rod (0.1 mm). Data were collected on a heating ramp with stops at temperatures chosen in a 90–390 K range. At each temperature 2×30 s acquisitions (30° rotation) were collected for 8 detector positions, effectively covering 2θ range from 2 to 155 degrees. Synchrotron powder XRD was carried out on $La_{2.8}Ca_{0.2}Rh_4Sn_{13}$ at the Swiss-Norwegian Beamlines at the European Synchrotron Radiation Facility in Grenoble. The specimen was powdered and loaded into a 0.3 mm quartz capillary. The instrument was operated at wavelength 0.714 46 Å and the temperature was maintained using Cryostream 700+ temperature controller. The datasets were collected on a heating ramp with 6 K min^{-1}. The 2D images were processed using CrysAlis software package and full pattern Rietveld refinements were carried out using the Fullprof Suite [24]. Variable temperature ramps were merged, visualized and fit using the DAVE package [25].

Variable temperature Raman spectra were collected on a Horiba Yvon Jobin LabRAM HR instrument using a 531 nm laser and Linkam Examina THMS 600 cold stage. Measurements were performed using twenty integrations with a 6 s acquisition time with x50 long working distance objective and 600 lines per mm grating (giving a spectral resolution of 0.5 cm^{-1}) over a Raman shift range between 80 and 1200 cm^{-1}.

The compositions of the $Ca_{3-x}Ce_xRh_4Sn_{13}$ and $Ca_{3-x}La_xRh_4Sn_{13}$ samples, checked by electron microprobe technique (also by time-of-flight secondary ion mass spectrometry and by XPS analysis) were very close to the assumed stoichiometry, e.g., for $Ca_{2.2}La_{0.8}Rh_4Sn_{13}$ with assumed atomic concentration ratio 11:4:20:65, respectively we determined 11.51 at% Ca, 4.09 at% La, 19.79 at% Rh, and 64.61 at % Sn. However, local fluctuations in stoichiometry over the length of the sample were observed at the nanoscale for all x components of both systems, the greatest one exist for Ce or La, which explain the strong disorder induced by doping. The

[6] For $Sr_3Ir_4Sn_{13}$ the cubic *high temperature* structure has been obtained as I' phase with crystallographic symmetry $I\bar{4}3d$ [3]. Assuming this structural properties, Kuo *et al* [5] have speculated the possible modulation wave vector $\mathbf{q} = (1/2, 1/2, 1/2)$ to describe the physical low-T properties associated with Fermi-surface reconstruction of $Sr_3Ir_4Sn_{13}$.

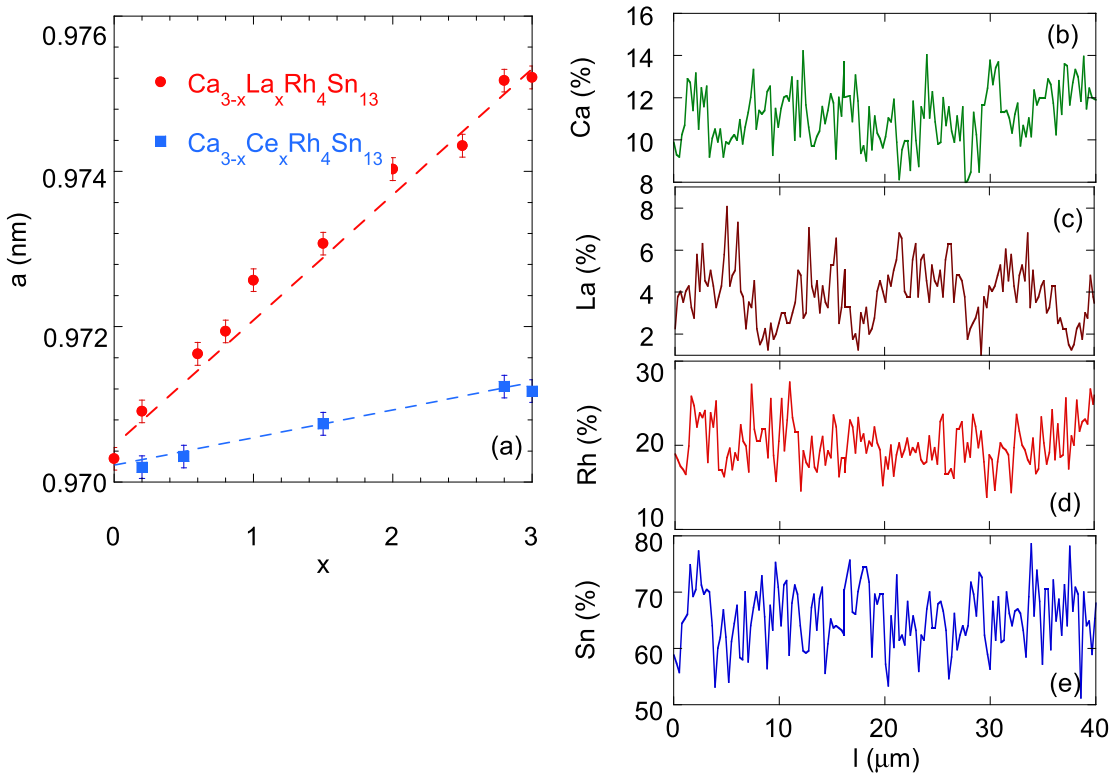

Figure 1. (a) The lattice parameter, a, plotted against La or Ce concentration, x, for the $Ca_{3-x}La_xRh_4Sn_{13}$ and $Ca_{3-x}Ce_xRh_4Sn_{13}$ series of alloys. The lattice parameters follow Vegard's law, which suggests good sample quality and stoichiometry of the components x. Panels (b)–(e) show variations in stoichiometry of Ca, La, Rh, and Sn, respectively over the length of the $Ca_{2.2}La_{0.8}Rh_4Sn_{13}$ sample.

detailed investigations of the homogeneity of the series of $Ca_{3-x}Ce_xRh_4Sn_{13}$ compounds are presented and discussed in [12], similar fluctuations in the composition are observed in the system of $Ca_{3-x}La_xRh_4Sn_{13}$ alloys (see panels (b)–(e) in figure 1), which signals site disorder.

Figure 1(a) displays the lattice parameters a versus x obtained at room temperature for $Ca_{3-x}La_xRh_4Sn_{13}$ and $Ca_{3-x}Ce_xRh_4Sn_{13}$ samples, with an error bar determined by the experimental accuracy of $\Delta\theta = 0.005°$ for each XRD pattern. For both cases a increases linearly with the increasing concentration of the dopant, although the La and Ce atomic radii are smaller than the Ca atomic radius. This behavior can be explained by different ionic radius of $Ca^{2+} \cong 1$ Å, $La^{3+} \cong 1.15$ Å, and $Ce^{3+} \cong 1.11$ Å, respectively, which suggests the localized character of f-electron bands and the localized magnetic moment of Ce.

Electrical resistivity ρ at ambient pressure and magnetic fields up to 9 T was investigated by a conventional four-point ac technique using a quantum design physical properties measurement system (PPMS). Measurements of ρ under pressure were performed in a piston-cylinder clamped cell (for details, see [26, 27]).

Specific heat C was measured in the temperature range 0.4–300 K and in external magnetic fields up to 9 T using a quantum design PPMS platform. The dc magnetization M and (dc and ac) magnetic susceptibility χ were obtained using a commercial superconducting quantum interference device magnetometer from 1.8 to 300 K in magnetic fields up to 7 T.

The XPS spectra were obtained with monochromatized Al K_α radiation at room temperature using a PHI 5700 ESCA spectrometer. The sample was broken under high vacuum better than 6×10^{-10} Torr immediately before taking a spectrum.

The refined lattice parameters shown in figure 1 and corresponding atomic positions were used in our band structure calculations. The band structure calculations were accomplished using fully relativistic full potential local orbital method (FPLO9-00-34 computer code [28]) within the local spin density approximation as well as ELK FP-LAPW/APW+lo code [29]. The exchange correlation potential V_{xc} was used in the form proposed by Perdew–Wang [30] in both cases. The number of k-points in the irreducible wedge of Brillouin Zone was 80. The results obtained from both methods were accomplished for the same V_{xc}, and as expected were essentially the same. The ELK-code was used for accurate calculations of the electron localization function (ELF), whereas the FPLO method was used to study the pressure effects on the electron density of states (DOSs) of the samples.

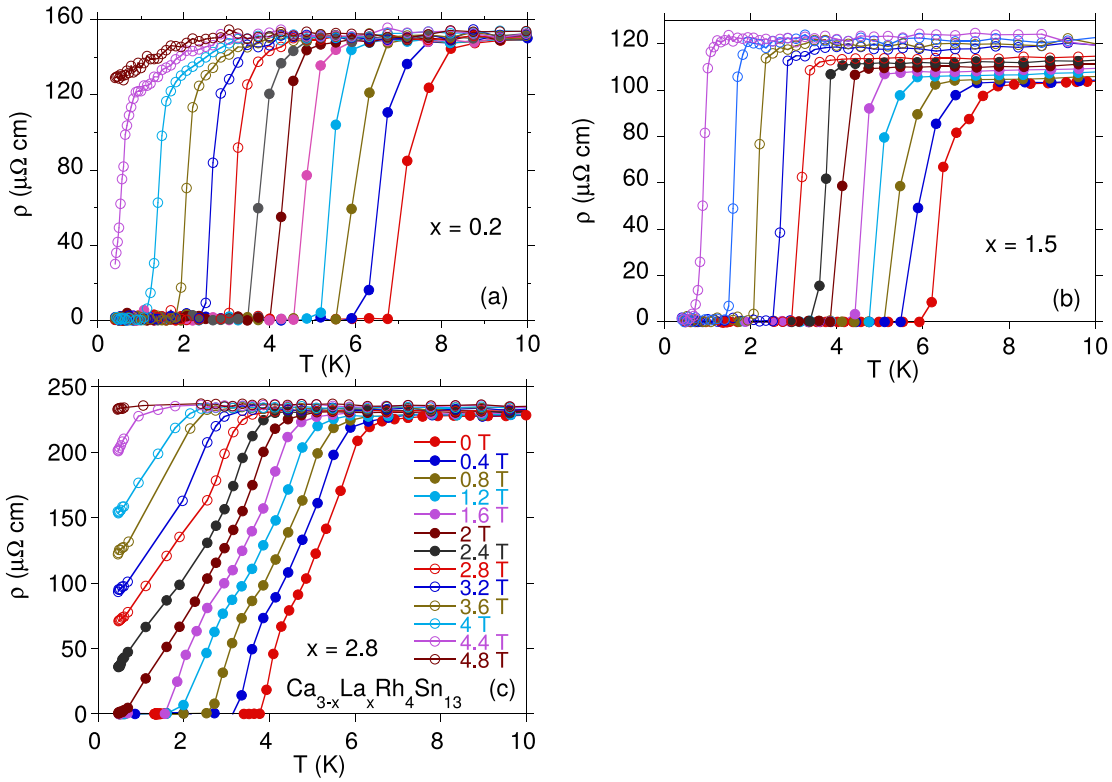

Figure 2. Electrical resistivity for $Ca_{1-x}La_xRh_4Sn_{13}$ ($x = 0.2$, 1.5, and 2.8) at various externally applied magnetic field for superconducting phases.

3. Results and discussion

3.1. Superconductivity in the presence of disorders in $Ca_3Rh_4Sn_{13}$ doped with La and Ce: a comparative study

3.1.1. Electrical resistivity; the effect of magnetic field and pressure on superconductivity

We expect that an increase of crystallographic disorder by doping of $Ca_3Rh_4Sn_{13}$ will enhance the separation of the $T_c^\star$ and T_c superconducting phases. We present a comprehensive magnetic and electrical resistivity study which indeed gives evidence of these two superconducting phases. Figure 2 displays temperature dependence of electrical resistivity $\rho(T)$ for $Ca_{3-x}La_xRh_4Sn_{13}$ with $x = 0.2$, 1.5, and 2.8 in various magnetic fields. Similar $\rho(T)$ dependencies versus B were very recently reported for the series of $Ca_{3-x}Ce_xRh_4Sn_{13}$ alloys [12]. The critical temperature $T_c^\star$ is defined as the temperature at which the resistivity falls to 50% of its normal state value. The transitions shown in figure 2 are much broader then that of $Ca_3Rh_4Sn_{13}$, which signals strong inhomogeneity due to the doping. The effect is so strong that for the alloys $x = 1.5$ and 2.8, $\rho(T)$ exhibits two distinct drops, which indicate a double resistive phase transition to the superconducting state, e.g., for the sample $x = 2.8$, the first resistivity drop is observed at ~5.3 K where isolated *superconducting islands* begin to be formed, while the second one is at lower temperature $T_c \sim 3.9$ K, where a global phase coherence develops with a limit of $\rho \to 0$. This complex transition is also seen in the ac susceptibility (see section 3.1.2). For Ce-substituted $x > 1$ samples, a large atomic disorder may have contributed to the formation of only the inhomogeneous superconducting phase (see the $T-H$ diagram in section 3.1.3). It is interesting to show whether the effect of disorder could also be observed in $\rho(T)$ data under external pressure, where pressure is another control parameter. Our investigations do not confirm this hypothesis (see figures 3, also figure 8 in [13], and figures 9 and 10 in [19]), which means that inhomogeneity is the direct cause of the $T_c^\star$ effect. Another interesting phenomenon is the observation of positive magnetoresistivity $\mathrm{MR} = [\rho(4T) - \rho(0)]/\rho(0)$ obvious near $T_c^\star$. At the critical temperature MR coefficient is about 20% for La-doped and about 90% for superconducting Ce-doped alloys. The positive magnetoresistivity can be interpreted as an effect of strong d-electron correlations [2, 31], which dominate the field-dependent electronic transport in this *nonmagnetic* material[7]. Figure 3 shows the electrical resistivity as a function of temperature for $Ca_{2.8}La_{0.2}Rh_4Sn_{13}$ and $Ca_{0.5}La_{2.5}Rh_4Sn_{13}$ under external pressure.

[7] The long range magnetic order has not been observed for x components of $Ca_{3-x}Ce_xRh_4Sn_{13}$ in temperatures $T > 0.4$ K, however, presence of short-range magnetic correlations with spin-glass-like behavior are confirmed by ac magnetic susceptibility data, magnetization M versus B, and specific heat.

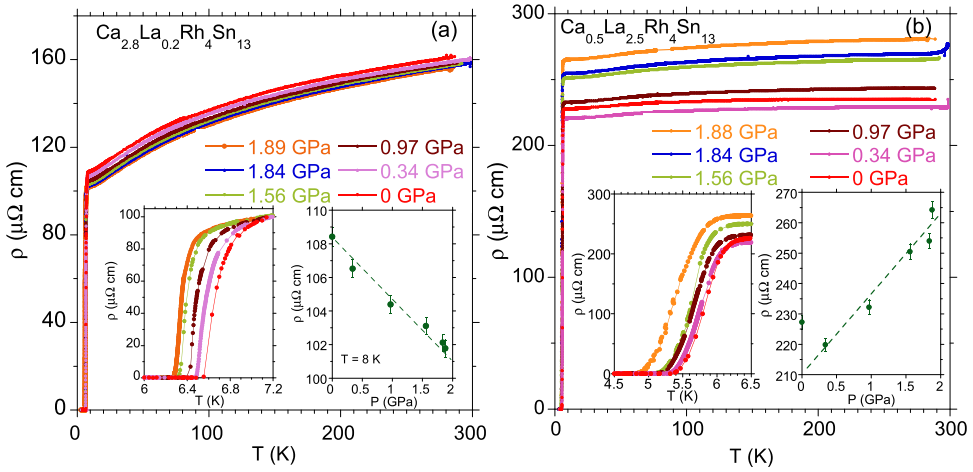

Figure 3. (a) Electrical resistivity for $Ca_{2.8}La_{0.2}Rh_4Sn_{13}$ under applied pressure. The left inset shows details of the superconducting transition under pressure, the right inset displays the value of ρ measured just above $T_c^\star$ at $T = 8$ K. (b) The same for $Ca_{0.5}La_{2.5}Rh_4Sn_{13}$. The left inset shows details of the superconducting transition under pressure, the right inset displays the value of ρ measured just above $T_c^\star$ at $T = 7$ K.

From these data we obtained the pressure coefficients $\frac{dT_c^\star}{dP} = -0.19$ K GPa^{-1} for $Ca_{2.8}La_{0.2}Rh_4Sn_{13}$ and -0.21 K GPa^{-1} for $Ca_{0.5}La_{2.5}Rh_4Sn_{13}$, respectively. Very similar pressure coefficients of $T_c^\star$ are: -0.2 K GPa^{-1} for $Ca_3Rh_4Sn_{13}$ and -0.3 K GPa^{-1} for the $x = 0.2$ cerium doped sample [12]. These coefficients $\frac{dT_c^\star}{dP}$ are significantly larger than the pressure coefficients of T_c, found in similar isostructural La-based superconductors [19], e.g., $\frac{dT_c}{dP}$ is only -0.05 K GPa^{-1} for $La_3Rh_4Sn_{13}$ [13]. The P-dependence of T_c can be interpreted according to the Eliashberg theory of superconductivity [32] and the McMillan expression [33, 34],

$$T_c = \frac{\theta_D}{1.45} \exp\left\{\frac{-1.04(1+\lambda)}{\lambda - \mu^*(1+0.62\lambda)}\right\}, \quad (1)$$

as a solution to the finite-temperature Eliashberg equations, where λ is the electron–phonon coupling parameter, and the Coulomb repulsion $\mu^\star$ is assumed to be ~0.1 which is a typical value known for s and p band superconductors. Our estimation gives $\lambda \approx 0.62$ for T_c phase of $Ca_3Rh_4Sn_{13}$, and slightly higher value of $\lambda^\star \approx 0.63$ for its inhomogeneous $T_c^\star$ phase. For $La_3Rh_4Sn_{13}$ $\lambda \approx 0.52$, while $\lambda^\star \approx 0.59$. Since the coupling λ given by the expression [33, 35]

$$\lambda = \frac{N(\epsilon_F)\langle I^2\rangle}{M\langle\omega^2\rangle}, \quad (2)$$

where $\langle I^2\rangle$ is the square of the electronic matrix element of electron–phonon interactions averaged over the Fermi surface, $\langle\omega^2\rangle$ is an average of the square of the phonon frequency ($\omega \sim \theta_D$), $N(\epsilon_F)$ is a DOSs at the Fermi energy, and M is the atomic mass, is larger for the inhomogeneous superconducting $T_c^\star$ state with respect to the bulk effect observed below T_c, the primary reason for $\frac{dT_c^\star}{dP} > \frac{dT_c}{dP}$ is the pressure dependence of θ_D, which leads to larger lattice stiffening in the $T_c^\star$ phase with respect to the bulk effect below T_c and contributes to the $T_c^\star > T_c$ effect. The P dependence of θ_D is given by the Grüneisen parameter $\gamma_G = -\frac{d\ln\theta_D}{d\ln V}$, which determines the lattice stiffening. It was documented experimentally [36] that γ_G strongly determines the magnitude and sign of $\frac{dT_c}{dP}$. In the case of inhomogeneous superconductivity one can also suppose the dominant impact of the pressure dependence of the DOS at the Fermi level, ϵ_F, more pronounced than in bulk superconducting phases.

Figure 4 shows the $H - T$ phase diagram of the $Ca_{3-x}La_xRh_4Sn_{13}$ and $Ca_{3-x}Ce_xRh_4Sn_{13}$ alloys, respectively. Temperatures $T_c^\star$ were obtained from the resistivity data, while T_c were obtained from the specific heat measurements. The Ginzburg–Landau (GL) theory fits well the data as is shown in the $H - T$ plots in figure 4. The best fit of the GL equation $H_{c2}(T) = H_{c2}(0)\frac{1-t^2}{1+t^2}$, where $t = T/T_c$ gives the upper critical field values of $H_{c2}(0)$ and $H_{c2}^\star(0)$, where $H_{c2}^\star(0) > H_{c2}(0)$, as shown in the figure 4. Moreover, a significant increase of $H_{c2}^\star(0)$ due to chemical doping has been documented in both lanthanum ($Ca_{3-x}La_xRh_4Sn_{13}$) and cerium ($Ca_{3-x}Ce_xRh_4Sn_{13}$) doped samples in respect to $H_{c2}^\star(0)$ of the parent compounds, e.g., $H_{c2}(0) \approx H_{c2}^\star(0)$ is about 3.1 T for $Ca_3Rh_4Sn_{13}$, 1.6 T for $La_3Rh_4Sn_{13}$, while $H_{c2}^\star(0)$ is ~4.3 T or ~3.8 T in $Ca_3Rh_4Sn_{13}$ substituted with La or Ce, respectively. Indeed, magnetization M versus B measurements and the residual resistivity ratio suggest an increase of $H_{c2}^\star(0)$ associated with a progressive change of atomic disorders. Within the weak-coupling theory [37], the expression $\mu_0 H_{c2}(0) = \frac{\Phi_0}{2\pi\xi(0)^2}$ gives the superconducting coherence length $\xi(0)$ or $\xi^\star(0)$

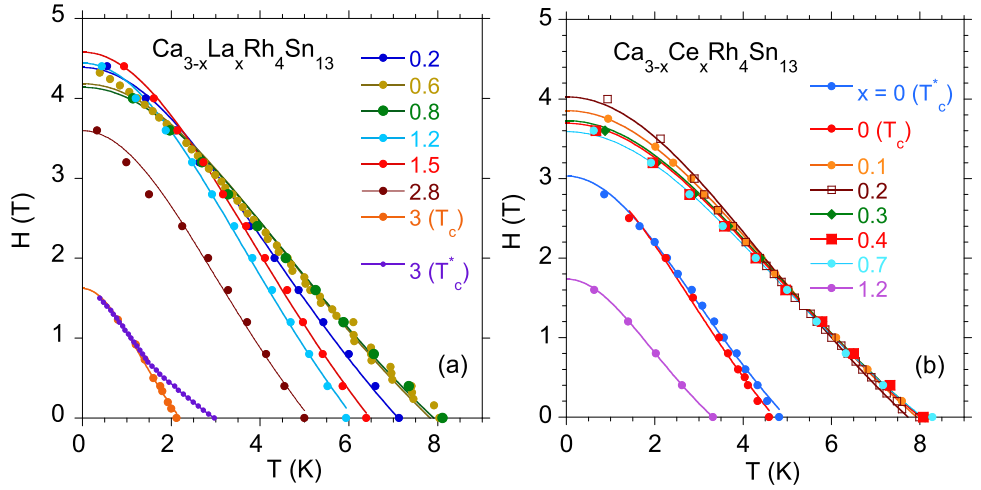

Figure 4. Temperature dependence of the upper critical field H_{c2} and/or $H^{\star}_{c2}(0)$ in the $H-T$ phase diagram, shown for $Ca_{3-x}La_xRh_4Sn_{13}$ in panel (a) and for $Ca_{3-x}Ce_xRh_4Sn_{13}$ in panel (b). $T^{\star}_c$ versus H data are obtained from electrical resistivity under H, and defined as the temperature at which ρ drops to 50% of its normal-state value. T_c versus H data for $Ca_3Rh_4Sn_{13}$ (in panel (b)) and for $La_3Rh_4Sn_{13}$ (in panel (a)) are obtained from $C(T)/T$ versus T data (see [12, 13]). The solid lines represent a fit using the GL model of $H_{c2}(T)$.

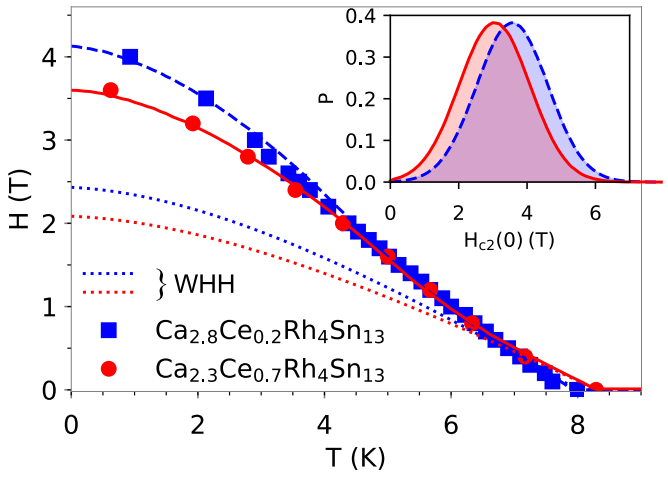

Figure 5. The upper critical field for $Ca_{3-x}Ce_xRh_4Sn_{13}$ for $x = 0.2$ and $x = 0.7$ fitted by results of a percolation model. The dotted lines show fits to the WHH model. The inset shows the distribution of the local H_{c2} assumed in the percolation model for $x = 0.2$ (dashed blue line) and $x = 0.7$ (solid red line).

($\Phi_0 = h/2e = 2.068 \times 10^{-15}$ T m^2 is the flux quantum). $Ca_3Rh_4Sn_{13}$ exhibits similar values of $\xi(0)$ and $\xi^{\star}(0) \cong 10.3$ nm (see [12]); for $La_3Rh_4Sn_{13}$, $\xi(0) \approx \xi^{\star}(0) \cong 14$ nm [13]. On the other hand, the value of $\xi^{\star}(0)$ depends on doping ($0 < x < 3$) and varies from 8.5 to 9.6 nm for the series of $Ca_{3-x}La_xRh_4Sn_{13}$ and from 9.0 to 13.7 nm for $Ca_{3-x}Ce_xRh_4Sn_{13}$ alloys, respectively with increasing of x (see figure 4).

From the theoretical point of view, the upper critical field in a dirty superconductor, where the free mean path $l \ll \xi$, can be described by the Werthamer–Helfand–Hohenberg (WHH) [38] or Maki–de Gennes [39] theories. The WHH theory gives

$$H_{c2}(0) = -0.69 \frac{\mathrm{d}H_{c2}}{\mathrm{d}T} T_c. \tag{3}$$

By comparing the experimental points and the dotted lines in figure 5 one can notice that these approaches underestimate $H_{c2}(T)$ at low temperatures. Moreover, they do not predict the positive curvature of $H_{c2}(T)$ close to T_c.

In figure 4 one can see that there is a *negative* correlation between the critical temperature and $H_{c2}(T = 0)$. Since, as can be seen in figures 1(b)–(e), the characteristic length of the spatial variation of the local doping level is much larger than the coherence length, one can assume that in the sample coexist regions with different T_c and $H_{c2}(T = 0)$. Then, the question is if this inhomogeneity can lead to the observed temperature dependence of H_{c2}

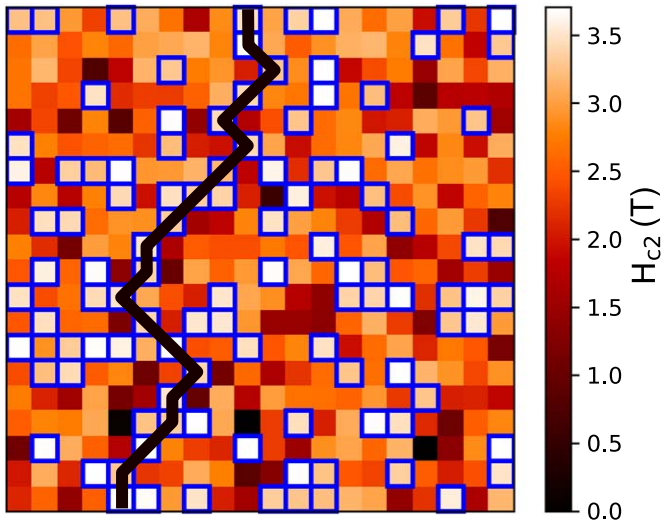

Figure 6. An example of the spatial distribution of local H_{c2}'s for a given realization of the doping inhomogeneity. The local H_{c2} in squares framed with blue line is higher than the external magnetic field. They form a superconducting path across the entire system, marked by thick black line, so the magnetic field is smaller or equal to the global $H_{c2}(T)$.

with a positive curvature in the high-T regime? It can be seen in figure 4(b) in [13] that a coexistence of high-T_c, low-H_{c2} and low-T_c, high-H_{c2} phases in $La_3Rh_4Sn_{13}$ leads to a kink in $H_{c2}(T)$. It is a tempting hypothesis that a continuous distribution of the local doping level and connected to it distribution of 'local $H_{c2}(T)$' lead to the observed shape of $H_{c2}(T)$. To verify such a possibility we constructed a toy model, where we assumed a square lattice composed of regions with a Gaussian distribution of local T_c's. For each of these regions we assume that the temperature dependence of H_{c2} is given by the WHH theory. We also assume that $H_{c2}(0)$ is a linear function of T_c with a negative coefficient. The global H_{c2} at a given temperature is then determined by the percolation threshold, i.e., when regions in the superconducting state form a continuous path across the entire system (see figure 6).

The results, presented in figure 5, were obtained in the following way: we assign T_c's (and corresponding $H_{c2}(0)$'s) randomly chosen from a Gaussian distribution to sites of a 100 $\times$ 100 square lattice. At each temperature T the external magnetic field is gradually reduced from $H_{c2}(0)$ to a value at which percolation occurs. This field defines $H_{c2}(T)$. Then, that value is averaged over 1000 realizations of the distribution of local T_c's. The model parameters are the relation between T_c and $H_{c2}(0)$ (given by dH_{c2}/dT at $T = T_c$ within the WHH theory) and the width of the Gaussian distribution of T_c's. In figure 5 one can see that the percolation model can very well reproduce the experimental data for $Ca_{3-x}Ce_xRh_4Sn_{13}$. The same is also possible for $Ca_{3-x}La_xRh_4Sn_{13}$ (not shown). However, the shape of $H_{c2}(T)$ given by the model is not universal and to obtain a good agreement with experimental results, the model parameters have to be fine tuned. In particular, it is necessary to assume a very wide spread of the 'local $H_{c2}(0)$', as presented in the inset in figure 5, and a strong negative correlation between T_c and $H_{c2}(0)$. For smaller spread or weaker correlation the positive curvature of $H_{c2}(T)$ usually takes place in the low temperature regime, in disagreement with the experimental data. Therefore, we cannot exclude that the inhomogeneity of the 'local T_c' combined with the negative correlation between T_c and $H_{c2}(0)$ is not the (only) reason for the particular shape of $H_{c2}(T)$ in these compounds.

One of the other possible explanations is multiband/multigap-nature of superconductivity. With the help of the quasiclassical Usadel equations [40, 41] it was shown in [42] that the upper critical field in a two-band superconductor can be determined as a solution of the following equation:

$$a_0[\ln t + U(h)][\ln t + U(\eta h)] + a_2[\ln t + U(\eta h)] + a_1[\ln t + U(h)] = 0, \quad (4)$$

where $U(x) \equiv \psi(x + 1/2) - \psi(1/2)$, $\psi(\ldots)$ is the di-gamma function, $t = T/T_c$, h is reduced magnetic field defined as $h = H_{c2}D_1/2\Phi_0 T$, D_1 is the band diffusivity, $\eta = D_2/D_1$. The parameters $a_{0,1,2}$ can be expressed by the intra-and interband BCS superconducting coupling constants λ_{11}, λ_{22}, λ_{12} and λ_{21}. The experimental data shown in figure 7 can be very well reproduced by fitting these parameters within the framework of the two-band/two-gap model.

This, however, is not solid proof of the multiband nature of superconductivity in $Ca_{3-x}La_xRh_4Sn_{13}$ and $Ca_{3-x}Ce_xRh_4Sn_{13}$. One reason is that there are so many fitting parameters in the model that the agreement with the experimental data is relatively easy to achieve. Other explanations for the deviation from the WHH theory are also possible. It is known that a positive curvature of $H_{c2}(T)$ can result from microscopic segregation in the superconducting material, where an array of Josephson junctions is formed [43–46]. In [12, 13] and [19] we

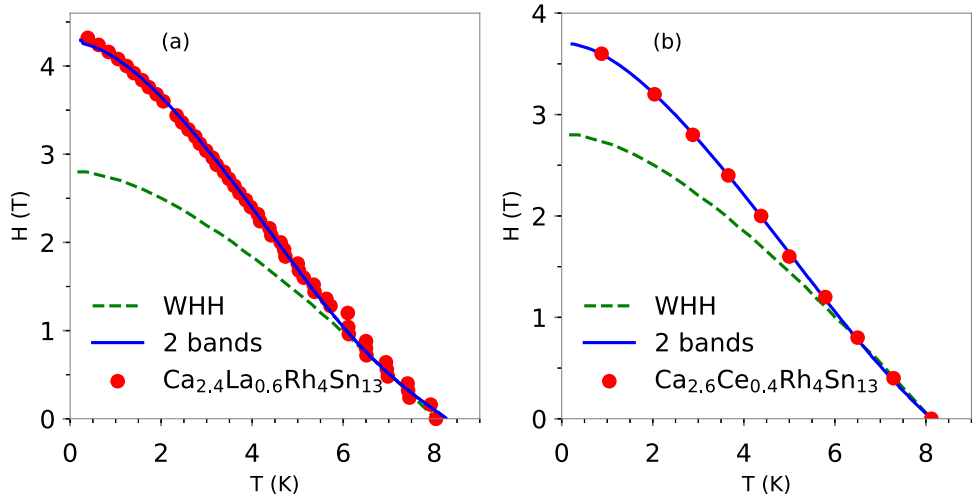

Figure 7. Examples of the upper critical field for La- (a) and Ce-doped (b) systems fitted by solutions of the WHH equations. The green dashed lines marked as 'WHH' show results of the WHH model with a single gap, whereas the solid blue lines marked as 'two bands' represent a two-gap model described in [42].

demonstrated the presence of two superconducting transitions due to the existence of inhomogeneous phase with $T^\star$ that is different from the T_c of the bulk sample. The first one corresponds to the onsets of an inhomogeneous phase where superconductivity is present only in a fraction of the volume and the second one that signals the onset of bulk superconductivity. Arguments for this scenario can also be seen in figure 2(c), where a double transition, characteristic for inhomogeneous superconductors [47] and suggesting the presence of microscopic segregation, can be seen. Other explanations of the shape of $H_{c2}(T)$ are related to the presence of magnetic impurities [48–50], strong quantization of Landau orbits [51, 52], inhomogeneity-induced reduction of the diamagnetic pair-breaking [53] or singularities in the DOSs [54].

3.1.2. Magnetic properties, evidence of short range magnetic order in Ce-doped alloys and the superconducting state

The superconducting state of $Ca_3Rh_4Sn_{13}$ is strongly dependent on the atomic disorder, which, upon quenching, leads to a significant decrease in T_c [10, 11]. Our simple model explains this observation based on the assumption that the atomic disorder leads to local stress [12]. We have calculated the systematic decrease of the DOSs at the Fermi energy with pressure [12] and documented for $Ca_3Rh_4Sn_{13}$ obtained under various technological treatment, that the DOS change correlates well with this decrease of T_c. According to this model, even a slight change in the DOS at ϵ_F may cause a significant change in T_c. With this motivation, we present a magnetic study of $Ca_3Rh_4Sn_{13}$ substituted with La and Ce to demonstrate evidence of nanoscale disorder as a bulk property, leading to an inhomogeneous superconducting state with an enhanced critical temperature $T_c^\star > T_c$. Here, $T_c^\star$ represents a drop of resistivity due to formation of percolation paths, while T_c determined from magnetic susceptibility and specific heat, indicates the onset of bulk superconductivity. A comparative study has shown, that the effect of short-range magnetic correlations has a significant effect on T_c. Figure 8 compare frequency dependence of the real (χ') and imaginary (χ'') parts of ac mass magnetic susceptibility χ_{ac}, and show derivative $d\chi'/dT$ and $d\chi''/dT$ for the selected $Ca_{3-x}Ce_xRh_4Sn_{13}$ samples and for $Ca_{0.5}La_{2.5}Rh_4Sn_{13}$, characteristic of the $Ca_{3-x}La_xRh_4Sn_{13}$ series.

Frequency ν dependencies in χ' and χ'', depicted in figure 8 with characteristic Vogel–Fulcher-like behavior [55] shown in the inset of panel (b), become apparent of spin-glass-like magnetic correlations in Ce doped alloys, while the ν effect is not observed for $Ca_3Rh_4Sn_{13}$ doped with La. The maxima in derivative $d\chi'/dT$ and $d\chi''/dT$ we assigned, respectively to critical temperatures $T_c^\star$ and T_c.

Figure 9 displays the magnetization M versus B isotherms for $Ca_{3-x}Ce_xRh_4Sn_{13}$ and $Ca_2LaRh_4Sn_{13}$ (a representative of the $Ca_{3-x}La_xRh_4Sn_{13}$ family). $Ca_{3-x}La_xRh_4Sn_{13}$ alloys are diamagnetic in the wide temperature region with hysteresis loops representing the effect of vortex pinning, while the $M(B)$ isotherms for $Ca_{3-x}Ce_xRh_4Sn_{13}$ are well approximated by Langevin function $L(\xi) = \coth(\xi) - \frac{1}{\xi}$, where $\xi = \frac{\mu B}{k_B T}$ with total magnetic moment $\mu \approx 0.8$–$0.9\ \mu_B$ per Ce atom obtained for the isotherms at 2 K. The hysteresis loop effect completely disappears for Ce content $x > 1$, the reason for this behavior is an atomic disorder leading to spin-glass-like magnetic correlations.

Figure 10 displays the specific heat data $C(T)/T$ and $\Delta C(T)/T$ for selected $Ca_{3-x}La_xRh_4Sn_{13}$ compounds. The $\Delta C(T)/T$ defined as a difference between the C/T data measured at zero magnetic field and at a field of 5 T clearly shows the difference in $C(T)/T$ behavior for the T_c and $T_c^\star$ phase. There is no sharp transition at T_c in the

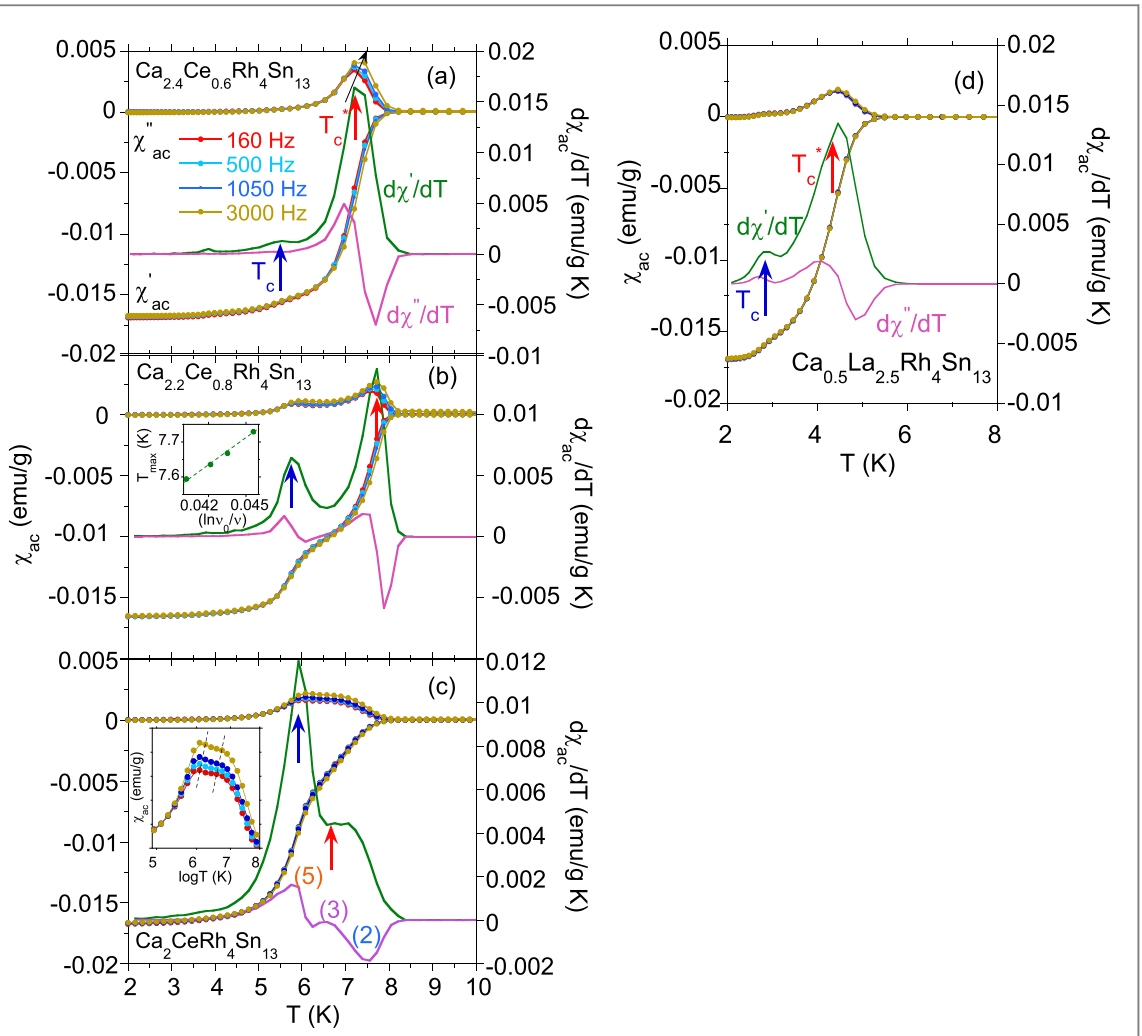

Figure 8. (a)–(c) The real and imaginary components of the ac magnetic susceptibility, χ' and χ'', for $Ca_{3-x}Ce_xRh_4Sn_{13}$, as a function of temperature measured at different frequencies in a field $B = 2$ Oe. The derivative $d\chi'/dT$ and $d\chi''/dT$ are also presented. The inset to panels (b) and (c) shows how χ'' depends on frequency with evidence of the spin-glass state. The minimum (2) of $d\chi''/dT$ exhibits the temperature at which the inhomogeneous superconducting phase is formed, while the maxima (3) and (5) defines temperature $T_c^\star$ and T_c, respectively (see also $T - x$ diagram in section 3.1.3). (d) The real and imaginary components of the ac magnetic susceptibility, χ' and χ'', for $Ca_{0.5}La_{2.5}Rh_4Sn_{13}$, as a function of temperature measured at different frequencies in a field $B = 2$ Oe. Also are presented the derivative $d\chi'/dT$ and $d\chi''/dT$. The frequency dependence characteristic of the spin-glass-like phase is not detected for the components x of $Ca_{3-x}La_xRh_4Sn_{13}$. The interpretation of $d\chi''/dT$ is similar to that, shown in panels (a)–(c). In all panels the vertical red and blue arrows indicate $T_c^\star$ and T_c, respectively.

specific heat data of the sample with $x = 0.2$; instead, the specific heat displays a broad peak below T_c, which is strongly reduced by field. This $C(T)$ effect was attributed to the inhomogeneous *high temperature* superconducting $T_c^\star$ phase due to atomic disorder [13, 19]. It has been shown in [56] that potential disorder smooth on a scale comparable to the coherence length leads to large modulation of the superconducting gap and large transition width[8]. A simple Gaussian gap $\tilde{\Delta}$ distribution [13]

$$f(\tilde{\Delta}) \propto \exp\left[-\frac{(\tilde{\Delta} - \tilde{\Delta}_0)^2}{2D}\right], \tag{5}$$

where $\tilde{\Delta}_0$ and D are treated as fitting parameters, fits well the $\Delta C(T)/T$ data for strongly disordered $Ca_{2.8}La_{0.2}Rh_4Sn_{13}$ alloy. The maximum of $f(\tilde{\Delta})$ distribution agrees well with the temperature of the χ'' maximum (3) in figure 8(d). The $C(T)/T$ data for rich in La $Ca_{3-x}La_xRh_4Sn_{13}$ compounds exhibit two superconducting phases (as shown in figure 10): the *high temperature* inhomogeneous superconducting $T_c^\star$ phase and the bulk superconducting state below T_c, where $T_c^\star > T_c$. Recently we noted that the $C(T)$ data for

[8] In reference to [17], a double superconducting transition, which appears in the good $PrOs_4Sb_{12}$ single crystals, with the best residual resistivity ratio $RRR_{2K} = 24$ and high jump at the superconducting transition, shows that its occurrence is phenomenon related to inhomogeneity within the size smaller than the size of investigated sample (100 μm). The $PrOs_4Sb_{12}$ samples that exhibit a double transition are most likely divided into macroscopically segregated parts: one with a large distribution of $T_c^\star$ and the other one with a single sharp superconducting transition at T_c, which seems to be intrinsic one.

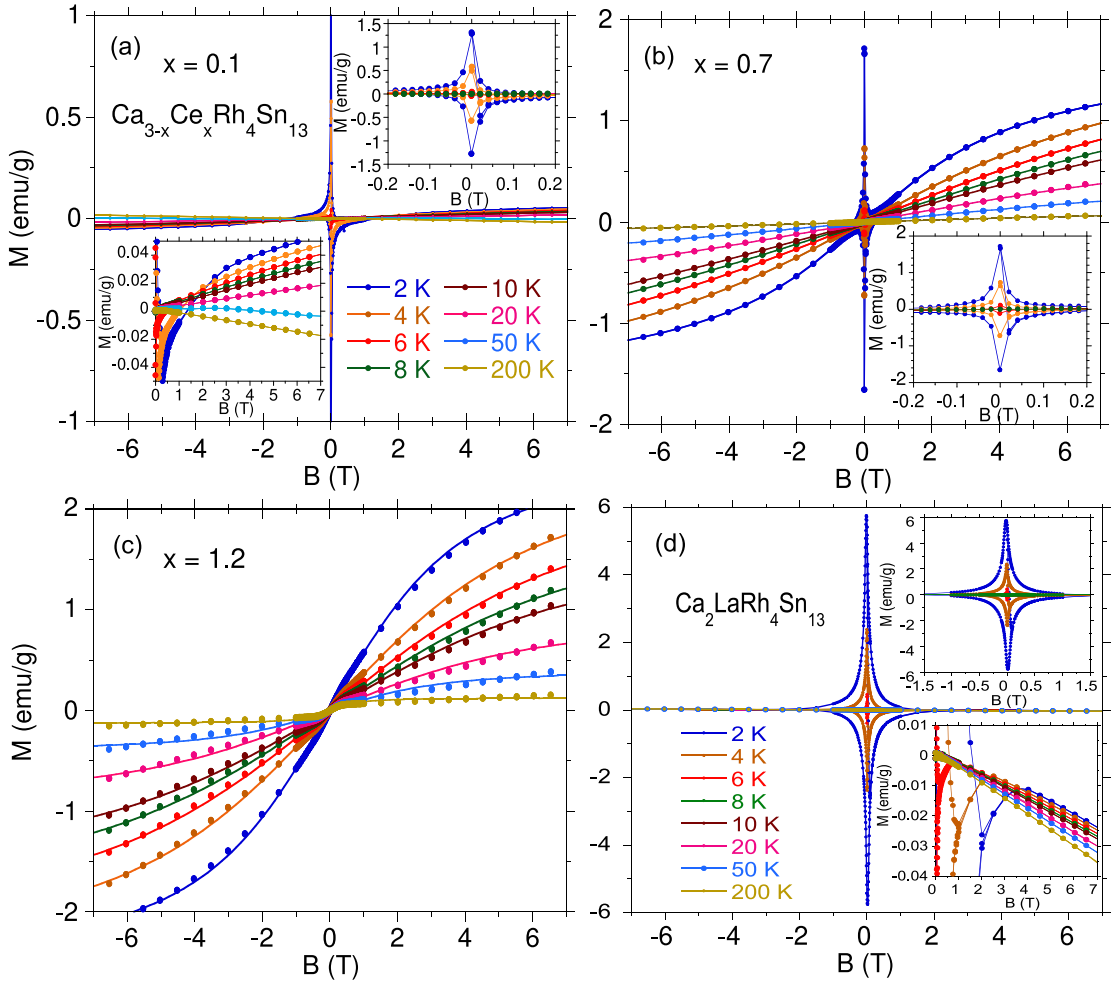

Figure 9. (a)–(c) Magnetization M versus magnetic field B for $Ca_{3-x}Ce_xRh_4Sn_{13}$ at different temperatures. The insets exhibit hysteresis loops for superconducting state observed for the components $x < 1.2$. A broad hysteresis loop suggests strongly inhomogeneous material. For $x \geqslant 0.4$ the solid lines are fits of the Langevin function to the magnetization. (d) Magnetization M versus magnetic field B isotherms for $Ca_2LaRh_4Sn_{13}$ at different temperatures. Similar M versus B isotherms are observed for remaining $Ca_{3-x}La_xRh_4Sn_{13}$ compounds. The insets exhibit hysteresis loops for superconducting state and the diamagnetic $M(B)$ behavior, respectively. A broad hysteresis loop suggests strongly inhomogeneous material.

$La_3Rh_4Sn_{13}$ [13] and $Ca_3Rh_4Sn_{13}$ [12] are well estimated by $C(T) \sim \exp\left[-\frac{\Delta(0)}{k_BT}\right]$, which indicates that these parent compounds are *s*-wave superconductors and follows the behavior described by the BCS theory in the weak-coupling limit ($\Delta(0)$ is the energy gap of T_c phase at zero temperature). The $C(T)$ data of cerium doped ($Ca_{3-x}Ce_xRh_4Sn_{13}$) samples were recently reported in [12]. It was documented [12] that the broad maximum observed at $T < T_c$ in the specific heat data of the samples $0 < x < 1.2$ represents an inhomogeneous superconducting phase in presence of spin-glass-like state, with evident contribution of the short-range magnetic correlations to entropy. Figure 11 compares the entropy of $Ca_{3-x}Ce_xRh_4Sn_{13}$ alloys with that of nonmagnetic La-doped alloys. Panel (b) displays the magnetic entropy S which for $x \geqslant 0.8$ has a linear scaling with x (panel (c)), and is $R\ln 2$ per Ce atom at about 6–7 K, indicating that the entropy represents the behavior of the ground state doublet. Figure 12 displays S versus x isotherms for Ce (panel (a)) and La (panel (b)) alloys. The $S(x)$ isotherms of $Ca_{3-x}Ce_xRh_4Sn_{13}$ are plotted at different temperatures T larger than the temperature of spin-glass-like ordering. For $x = 0.3$ and 0.8 when $Ca_3Rh_4Sn_{13}$ is substituted by Ce, and for $x = 0.6$ and ~2 for La doping, the isotherms $S(x)_{T=\text{const}}$ show a clear maxima that correspond to the largest separation between the superconducting phases $T_c^\star$ and T_c due to atomic disorder, as is displayed in $T - x$ diagram (will be discussed in section 3.1.3). In addition, $S(x)_{T=\text{const}}$ tends to increase with Ce substitution, which can easily be explained as a result of the x dependent paramagnetic spin-disorder effect (see figure 9). This behavior was not observed for the *nonmagnetic* La-doped series of alloys, as is shown in figure 12(b).

3.1.3. $T_c - x$ phase diagrams for $Ca_3Rh_4Sn_{13}$ doped with La and Ce

In summary, we present in figure 13 $T - x$ diagram of the superconducting $T_c^\star$ and T_c phases for $Ca_3Rh_4Sn_{13}$ doped with La (panel (a)) and Ce (panel (b)). The comprehensive magnetic, electrical resistivity, and specific heat

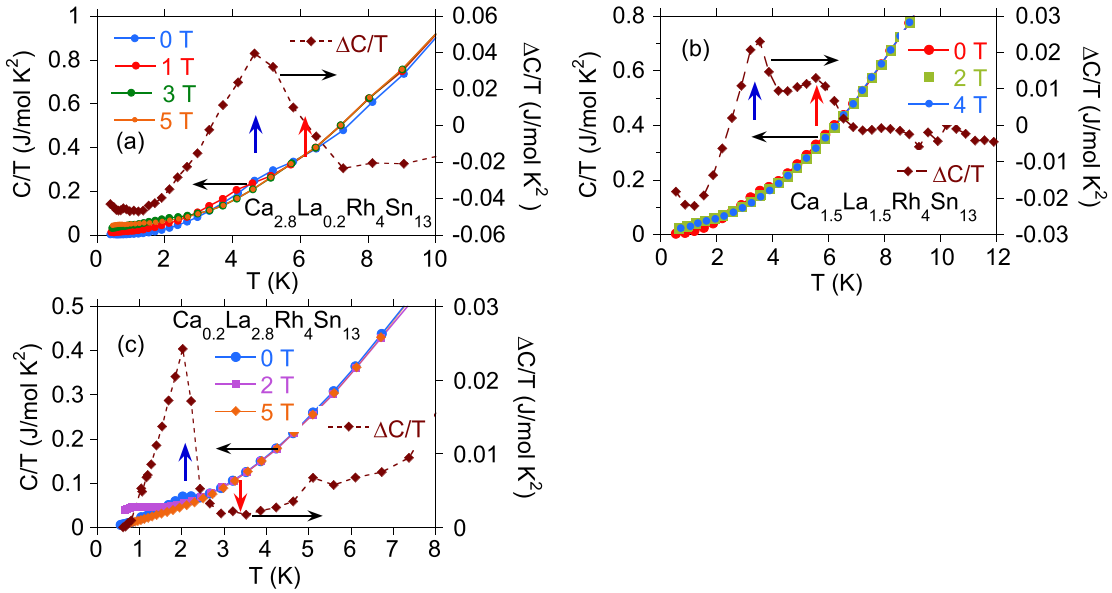

Figure 10. Temperature dependence of specific heat, $C(T)/T$ and $\Delta C(T)/T$, for $Ca_{3-x}La_xRh_4Sn_{13}$ in various magnetic fields. $\Delta C(T)/T$ is a difference of the $C(T)/T$ data obtained at the zero magnetic field and the field $B = 5$ T. For $Ca_{2.8}La_{0.2}Rh_4Sn_{13}$ (a), $\Delta C(T)/T$ has only one broad maximum, well approximated by the function $f(\tilde{\Delta})$, while the components $x \geqslant 0.6$ clearly show in the $\Delta C(T)/T$ data two maxima due to presence of $T_c^\star$ and T_c superconducting phases (in panels (b) and (c)). In all panels the vertical red and blue arrows indicate $T_c^\star$ and T_c, respectively.

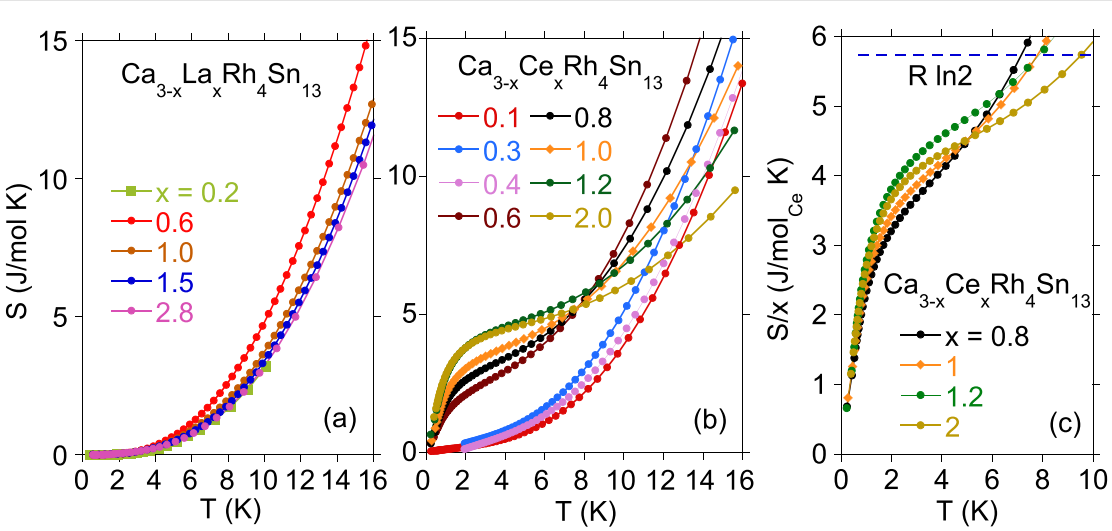

Figure 11. Entropy S of the samples $Ca_{3-x}La_xRh_4Sn_{13}$ (a) and $Ca_{3-x}Ce_xRh_4Sn_{13}$ (b) versus temperature at zero magnetic field B. Panel (c) shows that for for $T < \sim 7$ K S scales linearly with x.

study suggest coexistence of short-range magnetic correlations with superconductivity in the Ce-doping regime $x < 1.2$ this is, however, not the case for $Ca_3Rh_4Sn_{13}$ doped with La. In figure 13 markers (1) are obtained at 50% of the normal state resistivity value (see figure 2). The temperatures of the respective maxima in $d\chi''/dT$ shown in figure 8 are presented as the markers (2), (3) and (5). The χ versus T dc magnetic susceptibility data obtained at 500 Oe in zero field and field cooling modes reveals the onset of diamagnetism and thermal hysteresis associated with the superconducting state below $T_c^\star$ (points (4)). Markers (6) represent the temperature of the maximum in $d\chi_{dc}/dT$, which is T of about 1/2 of the diamagnetic dc susceptibility drop. Finally, markers (7) and (8) represent $T_c^\star$ and T_c obtained from specific heat $C(T)/T$ data, respectively (see figure 10). The $T - x$ diagram clearly indicates the presence of two separate superconducting phases, $T_c^\star$ and T_c. An increase of atomic disorder enhances the separation between them and the largest one is obtained for the La substituted samples with $x \sim 0.6$ and for the Ce substituted $Ca_3Rh_4Sn_{13}$ alloys with $x \sim 0.3$. We also documented that spin-glass-like magnetic correlations increases $T_c^\star$ and T_c for the $Ca_{3-x}Ce_xRh_4Sn_{13}$ compounds with respect to $Ca_{3-x}La_xRh_4Sn_{13}$. This observation is interesting, and previously was motivated by theory [57, 58]. It was

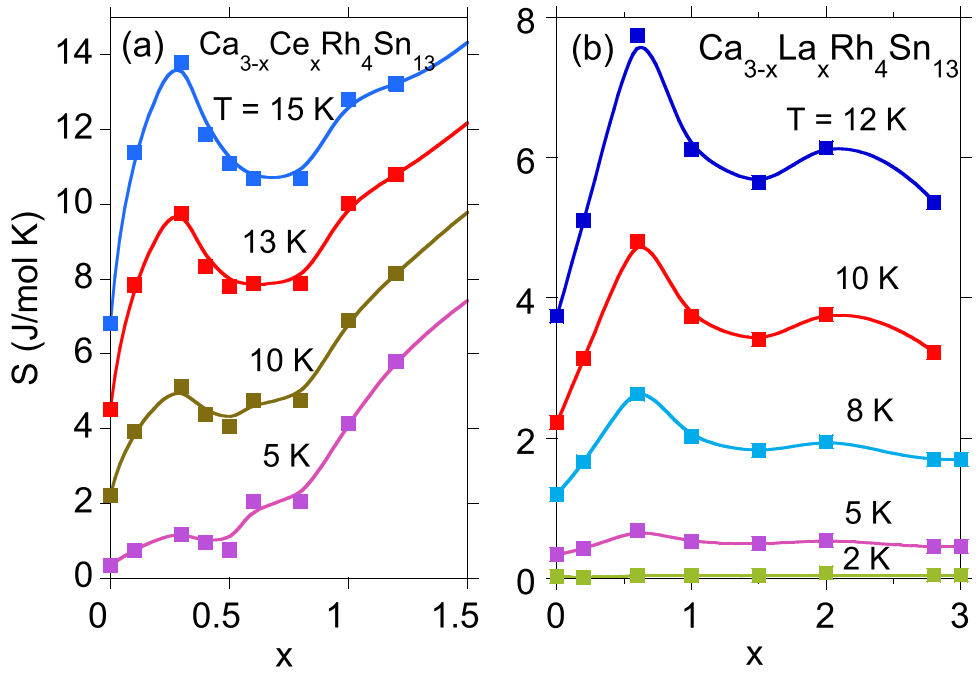

Figure 12. Entropy S isotherms as a function of doping x for $Ca_{3-x}Ce_xRh_4Sn_{13}$ (a) and $Ca_{3-x}La_xRh_4Sn_{13}$ (b) at different temperatures.

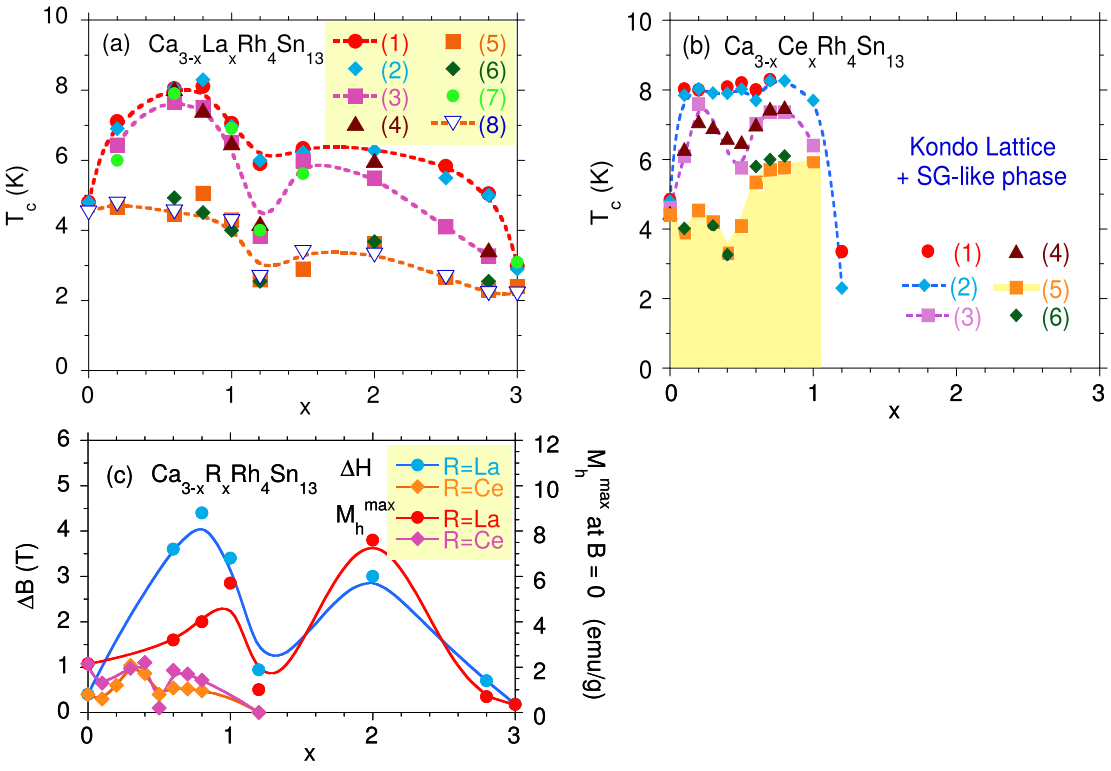

Figure 13. $T - x$ $T_c^\star$ and T_c phase diagram of $Ca_{3-x}La_xRh_4Sn_{13}$ (a) and $Ca_{3-x}Ce_xRh_4Sn_{13}$ (b) compounds from electrical resistivity (1), ac susceptibility (markers (2), (3), and (5)), dc magnetic susceptibility (makers (4) and (6)), and specific heat (markers (7) and (8)) measurements (details in the text). The dotted red curve represents the critical temperatures at which the $T_c^\star$ inhomogeneous superconducting phase begins to be formed. The purple dotted line represents the $T_c^\star$ inhomogeneous phases with superconducting gaps $\tilde{\Delta}_0$ corresponding to the maximum of Gaussian gap distribution $f(\tilde{\Delta})$. The critical temperatures T_c of the bulk superconducting phases are represented by the dotted orange line. Panel (c) shows details of the hysteresis loop effect in the superconducting regime; $|M_h^{\max}|$ is a maximum value of the magnetization M, and ΔB is the maximum field where the hysteresis loop is observed (see figure 9).

theoretically documented that the superconducting transition temperature is higher in the presence of the spin–spin interactions of the magnetic impurities, which form a spin-glass state.

The $T - x$ diagram also shows the minimum for T_c versus x dependence at $x_{\min} \sim 1.2$ for $Ca_{3-x}La_xRh_4Sn_{13}$, and at $x \sim 0.4$ for $Ca_{3-x}Ce_xRh_4Sn_{13}$, however, in the both cases $x_{\min}$ is about 40% of the whole superconducting x-region.

A detailed study of the electronic structure of $Ca_3Rh_4Sn_{13}$ doped with La and Ce are presented in appendix.

3.2. New insights into structural properties of $Ca_{3-x}La_xRh_4Sn_{13}$ and $Ca_{3-x}Ce_xRh_4Sn_{13}$ at high temperatures

A signature of the structural transition is associated with a change of symmetry, which is usually accompanied by appearance of additional reflections (satellites) as it was previously reported for many similar systems [5, 8, 59, 60]. Two scenarios have been suggested so far for structural deformations in 3:4:13 systems: (i) a CDW instability (e.g. $Sr_3Rh_4Sn_{13}$ [61] and $Sr_3Ir_4Sn_{13}$ [62]) or (ii) a phonon soft mode (PSM) [5, 59], both of which break symmetry and generate additional reflections. A clear evidence of the phonon softening was obtained directly from phonon dispersion curves [59]. On the other hand, CDW is usually identified from a spectral shifts of reflectivity [61, 62], which might be associated with other mechanisms. However, an important role of CDW as a precursor for superconductivity has already been theoretically outlined earlier by Caprara *et al* [22, 23] and very recently supported experimentally [21], therefore such scenario must also be taken into account. Critical temperatures of the soft phonon transitions are spread over a wide range from 350 K for $Ce_3Rh_4Sn_{13}$, 311 K for $La_3Rh_4Sn_{13}$, down to 38 K for $Ca_3Ir_4Sn_{13}$, while the reported CDW [61, 62] appears around 150 K. Therefore it is feasible that both mechanism PSM and CDW might be active in the same material but the structural transition (superstucture evidenced by satellites) will be *assigned* to the one with the higher transition temperature.

There has been only two types of structural transitions reported in the 3:4:13 systems related to the appearance of structural modulation with: (i) a single arm [63] or (ii) a whole k-star [59, 64] of the same, single propagation vector $k = \left(\frac{1}{2}, \frac{1}{2}, 0\right)$[9]. Transition temperatures associated with an appearance of the superstructure, commonly called $T^\star$, were usually lower than 150 K and could be suppressed to QCP by doping [8].

The first round of temperature dependent XRD has been performed to screen for any similar effects in both series. As a starting crystallographic model, a simple cubic cell (SG $Pm\bar{3}n$ No. 223, without the superstructure) was selected and atom occupancies were constrained to the nominal values. Atom positions were chosen as La/Ca/Ce (6d) $\left(\frac{1}{4}, \frac{1}{2}, 0\right)$, Rh (8e) $\left(\frac{1}{4}, \frac{1}{4}, \frac{1}{4}\right)$, Sn1 (2a) (0, 0, 0), Sn2 (24 k) (0, y_{Sn2}, z_{Sn2}). All sites were refined with individual isotropic atomic displacement parameters (ADP) B_{iso}[10].

3.2.1. Ca–Ce series

In the $Ca_{3-x}Ce_xRh_4Sn_{13}$ system we have studied two compositions with $x = 1$ and $x = 2$. Figure 14 presents middle sections of the diffraction patterns, which clearly shows the presence of a possible transition for the Ce rich side (a) $x = 2$ and uniform patterns in the other case (b) $x = 1$. The experimental setup did not allow to observe any superstructure reflections. In all cases, the variations in the intensities of reflections were accompanied by a prominent changes in ADPs (figures 15(a) and (b)). Other parameters varied smoothly with temperature.

Evidence of a possible transition is clearly seen for $CaCe_2Rh_4Sn_{13}$, where a gradual loss of intensity occurs in the 250–300 K range (figure 14(a)). At the same time, the intensities for $Ca_2CeRh_4Sn_{13}$ monotonically decrease over the whole temperature range (figure 14(b)). The transition for the Ce rich material is clearly seen in Rietveld refinement as a gradual increase of ADPs (figure 15(a)), which is not present on a Ca rich side (b). It is impossible to determine only from the diffraction data, if the origin of the increase of ADPs is static (phase transition) or dynamic (rattling of the central Sn1) and complementary studies are under way. There are also no signatures of the low temperature transition T_D seen in resistance and susceptibility data. At this moment, it suggests that the transition at T_D is rather confined to electronic and not the crystal structure. On the other hand, the high temperature transition (with onset around 250 K and completed around $T_{HT} = 310$ K), is most likely connected or acts as a precursor to an appearance of a $2a \times 2a \times 2a$ superstructure observed in similar materials

[9] k-star is formed by all symmetry equivalent propagation vectors. For example, transition only with $k = \left(\frac{1}{2}, \frac{1}{2}, 0\right)$ can lead to a tetragonal structure $2a \times 2a \times a$. However, in a cubic symmetry $\left(\frac{1}{2}, \frac{1}{2}, 0\right)$, $\left(\frac{1}{2}, 0, \frac{1}{2}\right)$ and $\left(0, \frac{1}{2}, \frac{1}{2}\right)$ are equivalent to each other therefore they all can be involved in the transition leading to a cubic $2a \times 2a \times 2a$ supercell as is the case of $La_3Rh_4Sn_{13}$.

[10] Refinements of measurements carried out with Cu K wavelength (1.54 Å) require an absorption correction, which is very difficult to estimate for the applied geometry and results in negative values of ADPs. An attempt was made to apply a moderate cylindrical absorption correction ($\mu r = 3.0$) but it was not sufficient to fully correct the data. In this case, the values of ADP have wrong absolute values but their mutual relations and general trends are preserved.

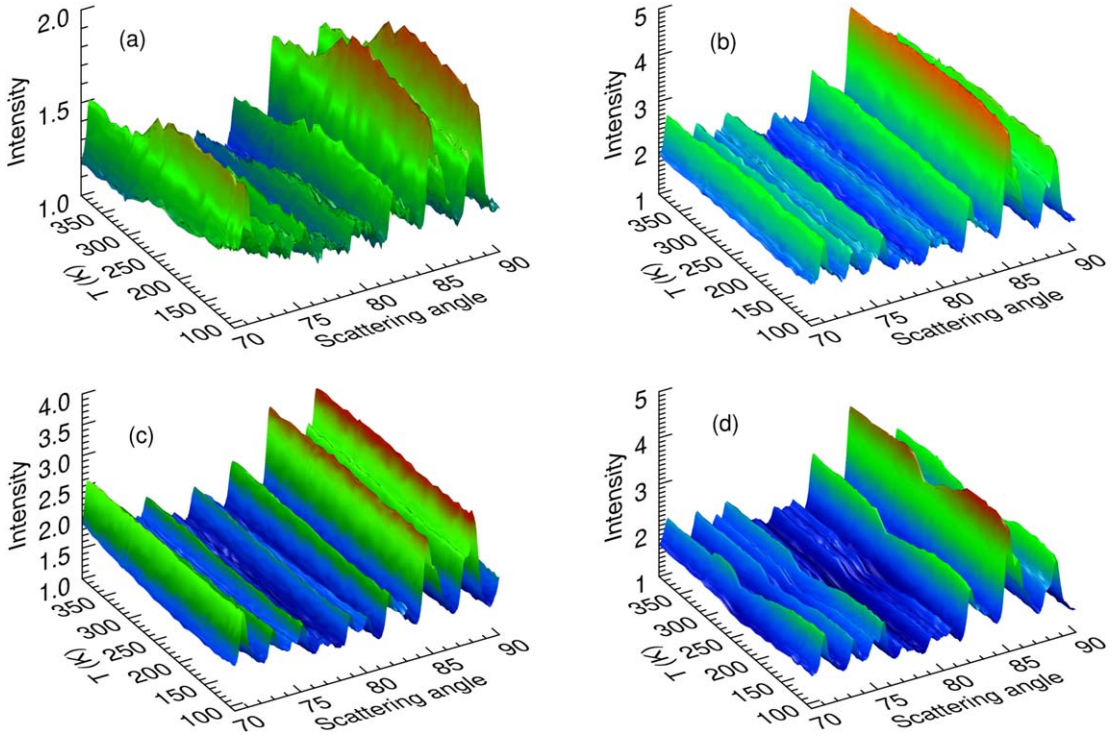

Figure 14. Temperature dependence of middle sections of diffraction patterns for (a) $Ca_1Ce_2Rh_4Sn_{13}$, (b) $Ca_2Ce_1Rh_4Sn_{13}$, (c) $Ca_1La_2Rh_4Sn_{13}$ and (d) $Ca_{2.8}La_{0.2}Rh_4Sn_{13}$.

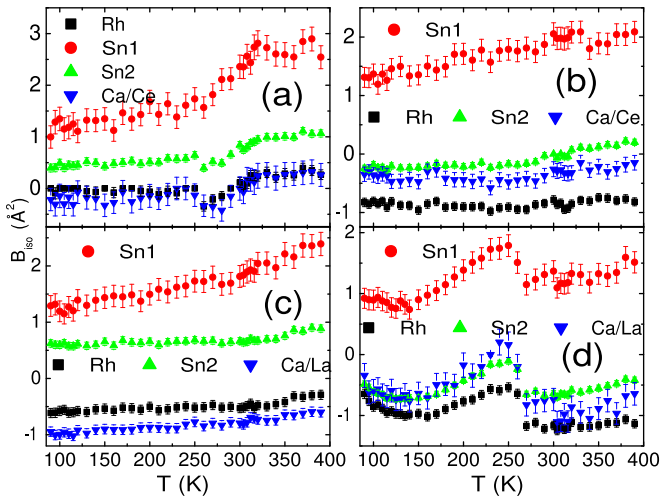

Figure 15. Temperature dependence of isotropic atomic displacement parameters (ADPs) for (a) $Ca_1Ce_2Rh_4Sn_{13}$, (b) $Ca_2Ce_1Rh_4Sn_{13}$, (c) $Ca_1La_2Rh_4Sn_{13}$ and (d) $Ca_{2.8}La_{0.2}Rh_4Sn_{13}$.

[8, 20, 59, 60, 63–65][11] which was below the detection limit for the Supernova setup. We can estimate that for $CaCe_2Rh_4Sn_{13}$ the T_{HT} lies between 310 and 320 K.

3.2.2. Ca–La series

In the Ca–La series a possible high temperature transition was observed around 250 K for $Ca_{2.8}La_{0.2}Rh_4Sn_{13}$ (figure 14(d)) but not for $CaLa_2Rh_4Sn_{13}$ (figure 14(c)). The refinement of the temperature dependence of ADPs for $Ca_{2.8}La_{0.2}Rh_4Sn_{13}$ (figure 15(d)) revealed 4 characteristic regions: (1) up to 140 K where ADPs anomalously decrease, (2) between 140 and 250 K where they increase as expected from increased thermal fluctuations, (3) a

[11] After the initial submission we have learnt that a transition similar to the one in $La_3Rh_4Sn_{13}$ has been observed in $Ce_3Rh_4Sn_{13}$ [60]. However, the paper reports only T^* around 350K and do not investigate any other structural signatures like variations in ADPs.

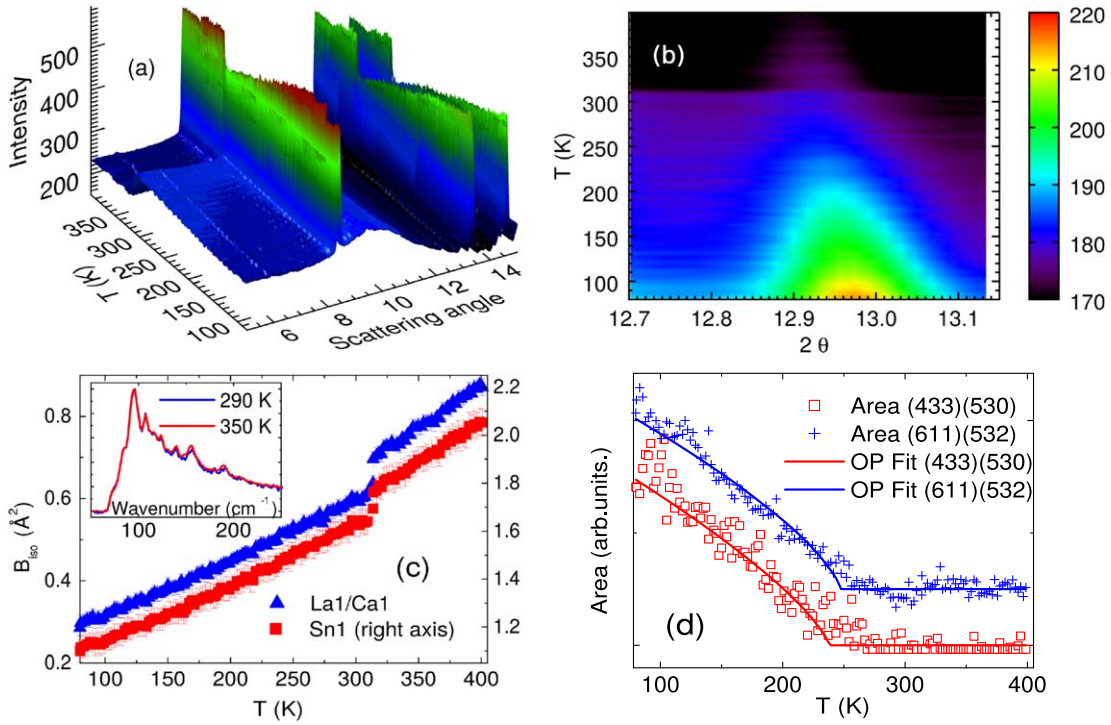

Figure 16. Low section of synchrotron PXRD diffractograms for $Ca_{0.2}La_{2.8}Rh_4Sn_{13}$ (a) shows gradual variation of intensities and (b) appearance of very low overlapping $2a \times 2a \times 2a$ superstructure peaks (532)(611). The variation of intensities is correlated with a sudden jump in B_{iso} at $T_{HT} = 310$ K (c), which does not affect Raman spectra (inset). On the other hand the superstructure reflections display critical behavior with $T^* \approx 250$ K (d).

sharp decrease around 250 K, which points towards sharp decrease of the disorder and (4) again a small step around 300 K. At this moment the increase of ADPs between 140 and 250 K can be attributed to an increase of a static disorder which contributes to atomic displacements equally with the thermal noise. This disorder is eliminated by an onset of a possible transition at 250 K, which is completed at around 300 K. Similarly to the $CaCe_2Rh_4Sn_{13}$, this increase is most likely associated (but does not have to coincide) with a structural transition which is below the detection limit of the current Supernova setup.

In order to justify the result, we present preliminary analysis of synchrotron PXRD carried out on $Ca_{0.2}La_{2.8}Rh_4Sn_{13}$ (figure 16), which lies on the La rich side of the Ca–La series and is expected to undergo the T^* transition. The low angle section of the pattern (figure 16(a)) reveals three important features: (1) a sudden drop of the background around 310 K, which is accompanied by an increase of peak intensity, which we attributed to a transfer of scattering intensity from a long range order represented by Bragg reflections to a short ranged component visible as diffuse scattering, (2) an appearance of $2a \times 2a \times 2a$ superstructure reflections (overlapping (532) and (611) in figure 16(b)), which decrease gradually with the temperature having a critical-like behavior below 250 K. An order parameter-like curve fitted for the stronger pair of reflections (figure 16(d)) gave better estimates of parameters: the $T^* = 247 \pm 19$ K and the critical exponent $\beta = 0.71 \pm 0.06$. We do not imply here that this transition is necessarily continuous but the quality of the fit and earlier reports on similar materials [8, 9] strongly support this conclusion. It must be noted that the intensity of the reflection is proportional to the $|F_{HKL}|^2$, which in the first approximation is proportional to the square of the deviation from the ideal symmetry. This means that the critical exponent calculated from intensities is twice as large as the one potentially calculated from the displacements (in a similar way intensities of magnetic peaks are proportional to the square of magnetic moment). Therefore the actual critical exponent of the order parameter will be equal to $\beta^* = 0.35 \pm 0.03$.

At the end, a quick look at representative ADPs (figure 16(c)) shows that the change in intensities of the main reflections and the jump of the background at $T_{HT} = 310$ K are connected to a displacive disorder. An attempt was done to differentiate between static and dynamic (increased rattling) origins of the transition by carrying out Raman measurements, in the energy range suitable for phonon excitations, at room temperature (below T_{HT} but above T^*) and 350 K (above T_{HT}), as is shown in figure 16(c) (inset). For better comparison a baseline was subtracted from both spectra and their respective maxima were normalized to 1. No significant difference in intensities is observed while crossing the 310 K boundary, therefore there is no evidence of sudden changes in vibrational/phonon modes, which would indicating a dynamic origin of the rapid change in the atomic

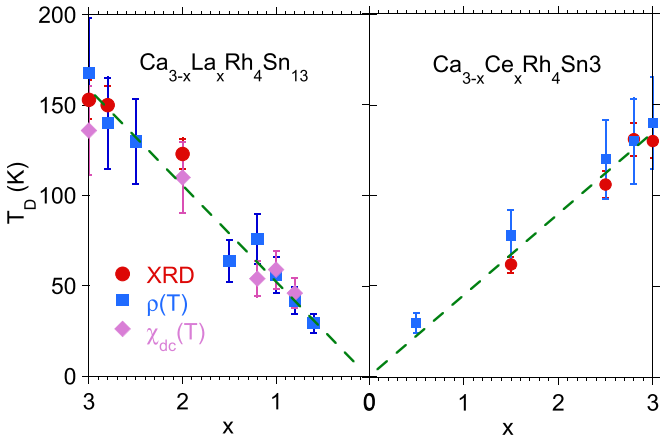

Figure 17. Phase diagram showing the effect of lanthanum ($Ca_{3-x}La_xRh_4Sn_{13}$) and cerium ($Ca_{3-x}Ce_xRh_4Sn_{13}$) doping on temperature T_D, which represents the change of the lattice dynamics of the respective alloys x (see the text, also [66]). The red points are the temperatures T_D, determined for each sample x from the d versus T plot in log–log scale. In such log−log presentation of the $d(T)$ data, T_D represents a clear kink between two linear dependencies in $d(T)$ at temperatures $T > T_D$ and $T < T_D$, respectively. The similar kink at T_D shows dc magnetic susceptibility $\chi_{dc}(T)$ (pink diamonds), and inverse electrical resistivity $1/\rho(T)$ (blue square points), when the both quantities are presented in log–log scale.

displacement parameters. It has to be noted that the phonon signature of the $\mathbf{q} = \left(\frac{1}{2}, \frac{1}{2}, 0\right)$ mode softening might be impossible to spot using Raman spectroscopy on a polycrystalline sample since optical spectroscopy probes predominantly the center of the Brillouin zone [$\mathbf{q} = (0, 0, 0)$]. A more plausible explanation of this transition is an appearance of a static disorder, which leads to a static long range ordered superstructure at lower temperatures.

The possible presence of an additional high temperature transition T_{HT}, which is associated with a sudden jump in ADPs and a decrease in a background seems to be a precursor to the long range order developed at T^* has not been previously reported in similar systems (see footnote 12). Our data shows that it is present in samples with $x_{La} = 0.2$ (figure 15(d)), $x_{La} = 2.8$ (figure 16(c)) and $x_{Ce} = 2.0$ (figure 15(a)) and is most likely connected with the appearance of short range correlations between atomic displacements. A striking feature for the Ca–La series is that it is visible for the border compositions $x_{La} = 0.2$ and $x_{La} = 2.8$ but not for $x_{La} = 2.0$[12].

One can ask if the transition T_D is somehow reflected in the structural properties. Due to limited angular resolution of Supernova scans, no subtle transitions could be detected in slopes of thermal expansion of lattice parameters and detailed studies are under way. For the purpose of this paper we have repeated the temperature scans with higher angular resolution over the angular range of the (622) reflection. Interplanar d-spacing calculated in this way was plotted on a log–log scale in a way similar to the resistance data. The plot revealed two possible inflection points with temperatures equivalent to T_D and T^*. At present we can only associate the lower transition with T_D since it perfectly correlates with temperatures observed in resistance and susceptibility data in both La and Ce doped series (figure 17). At this moment one can also argue that the T_D transition may be associated with a CDW-type instability, which is overimposed over a structure already deformed by an PSM mode with the same propagation vector. In this case, a CDW will not generate any additional reflections and a weak character of electronic order (a fraction of electron) will have neglible structural influence compared to shifts of heavy atoms like Rh or Sn. Additionally, this CDW does not have to be static but also might have a dynamic character as suggested in [23].

4. Conclusions

The comprehensive research on La and Ce substituted $Ca_3Rh_4Sn_{13}$ leads to several important observations, which are helpful for a better understanding of the nature of their superconductivity. The basic problem of our studies is an atomic disorder, which plays a crucial role in the strongly correlated materials. It was documented theoretically for this class of compounds that in the critical regimes near the QCP a system is at the threshold of an instability, and disorder as perturbation, can cause significant macroscopic effects. Due to structural disorder of the doped $Ca_3Rh_4Sn_{13}$, one has to distinguish between the two behaviors. First, the atomic disorder (not necessarily compositional) leads to significant decrease in T_c of $Ca_3Rh_4Sn_{13}$ upon quenching. This T_c decrease can easily be explained from the BCS equation [67] $T_c = \theta_D e^{-1/N(\epsilon_F)U}$ as consequence of local stress due to

[12] The compositions of the Ca rich sample was additionally checked by SEM after the XRD.

disorder, which significantly changes the $N(\epsilon_F)$ value, and thus changes the expression $N(\epsilon_F)U \sim \frac{\lambda-\mu^*}{1+\lambda}$ [68]. Secondly, the doping of $Ca_3Rh_4Sn_{13}$ generates the nanoscale electron disorder in the bulk sample, leading to an inhomogeneous superconductivity state with an enhanced critical temperature $T_c^\star > T_c$. The $T-x$ diagram (figure 13) and the entropy $S(x)_T$ isotherms (figure 12) document well the relation between degree of an atomic disorder and separation of two superconducting phases, $T_c^\star$ and T_c, in the T-scale. We interpret the effect of the high temperature $T_c^\star$ phase as a result of its larger lattice stiffening with respect to the bulk superconducting phase T_c. Based on the Eliashberg theory of BCS superconductivity and the band structure calculations, we propose a phenomenological model, which qualitatively describes the resistivity data obtained under high pressure.

We also demonstrated that the $T-x$ and $S(x)_T$ data correlate well with the appearance of a precursor disorder transition at $T_{HT} \sim 310$ K. This high-temperature phase transition is clearly observed for the $Ca_{3-x}La_xRh_4Sn_{13}$ and $Ca_{3-x}Ce_xRh_4Sn_{13}$ alloys having relatively low disorder due to doping, i.e., located in the $T-x$ diagram near the parent compounds $Ca_3Rh_4Sn_{13}$, $La_3Rh_4Sn_{13}$, or $Ce_3Rh_4Sn_{13}$, while for x-range, where the isotherms $S(x)_T$ show a maxima that correspond to the largest separation between the superconducting phases $T_c^\star$ and T_c the superstructure effect is missing. Therefore these structural effects are evidently linked to superconductivity of $Ca_3Rh_4Sn_{13}$ doped with La or Ce. The Rietveld refinement proves the *high temperature* structural transition T_{HT} connected to atomic disorder (ADPs), which subsequently leads to the long range superstructure at $T^\star$ and the subtle effects observed at T_D leave no structural signatures. However, the T_D can be associated with a CDW type instability (see [64]), and $T_D < T^\star < T_{HT}$. The both transitions have not been documented for parent $Ca_3Rh_4Sn_{13}$ compound. Typically, CDW competes with superconductivity, so in the range of small x value, CDW is a cause of a small difference in T_c of the inhomogeneous and homogeneous volume of the sample, as is shown in figure 13. As a result of an increase of doping, T_D increases (see figure 17), which leads to the appearance of the CDW phase. In the area of large disorder, structural deformations of T_{HT} or T_D-type are not visible, hence the difference between $T_c^\star$ and T_c is maximal. We also note that this precursor transition T_{HT} connected with strong variations of ADPs does not have to coincide (and in fact does not coincide for $x_{La} = 2.8$) with the appearance of the $2a \times 2a \times 2a$ superstructure, which has not been reported earlier in similar systems.

In such *dirty* $Ca_{3-x}La_xRh_4Sn_{13}$ and $Ca_{3-x}Ce_xRh_4Sn_{13}$ superconductors, where the mean free path is much smaller than the coherence length, the upper critical field $H_{c2}(T)$ is usually interpreted within the WHH or Maki–de Gennes theoretical model. This model, however, does not well fit the H_{c2} versus T_c data, and does not interpret the observed positive curvature of H_{c2} close to T_c. One of the possible scenarios of the observed $H_{c2}(T)$ dependencies is based on the presence of nanoscopic inhomogeneities of the superconducting state. To support this explanation we proposed a simple percolation model and demonstrated that it can very well reproduce the experimental data. However, since the model requires a set of fine-tuned parameters, we do not claim that it is the only possible explanation. Another possibility can be, e.g., a two-band nature of superconductivity in these systems. Previously, intriguing evidence for multiband effects was also documented in structurally similar filled skutterudite $LaRu_4As_{12}$ [69] and $LaOs_4As_{12}$ [70] compounds.

Acknowledgments

The research was supported by National Science Centre (NCN), Poland on the basis of Decision No. DEC-2012/07/B/ST3/03027. MMM acknowledges support by NCN under grant 2016/23/B/ST3/00647. PW acknowledges support by NCN under grant DEC-2015/17/N/ST3/02361. High-pressure research at the University of California, San Diego, was supported by the National Nuclear Security Administration under the Stewardship Science Academic Alliance program through the US Department of Energy under Grant Number DE-NA0002909. One of us (AŚ) is grateful for the hospitality at the University of California, San Diego (UCSD), and expresses his appreciation to the Kosciuszko Foundation for support during his visit. We are grateful to Dr D Chernyshov and Dr W van Beek from ESRF (Swiss Norwegian Beamlines) for help with diffraction measurements.

Appendix. Electronic structure of $Ca_3Rh_4Sn_{13}$ doped with La and Ce; experiment and calculations

In order to explain the alloying effect on the band structure of $Ca_3Rh_4Sn_{13}$ superconductor, we investigated valence-band (VB) XPS spectra of the $Ca_{3-x}La_xRh_4Sn_{13}$ and $Ca_{3-x}Ce_xRh_4Sn_{13}$ samples. Figure A1 shows the VB XPS spectra for the series of $Ca_{3-x}La_xRh_4Sn_{13}$ alloys. The XPS bands for the components $x = 0, 0.5, 2.5$, and 3 are compared with calculated total DOSs. Panel (c) displays also the VB XPS spectra obtained for intermediate components $0.5 < x < 2.5$. The valence band XPS spectra of $Ca_{3-x}Ce_xRh_4Sn_{13}$ alloys were recently presented

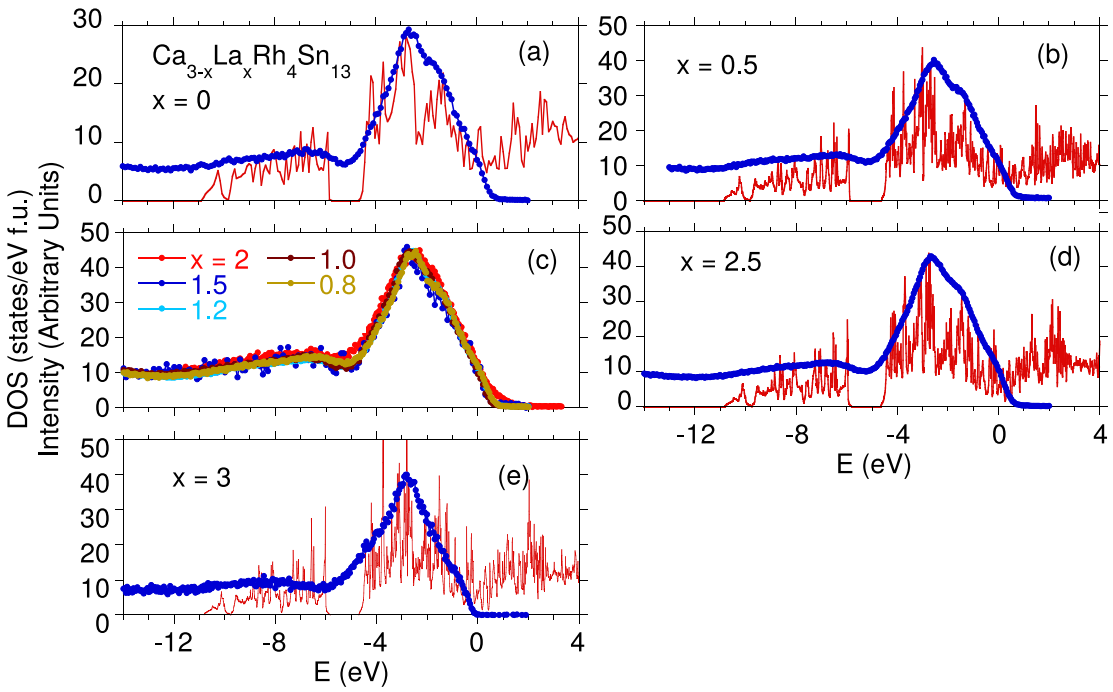

Figure A1. Valence band XPS spectra for $Ca_{3-x}La_xRh_4Sn_{13}$ compared with the calculated total density of states within the LSDA approximation (narrow red line) for the components $x = 0, 0.5, 2.5$, and 3. The figure also shows the VB XPS spectra for intermediate components of the series (in panel (c)).

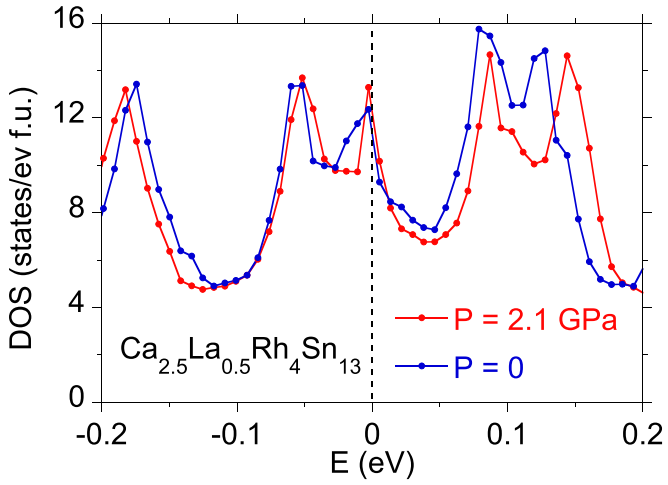

Figure A2. The total DOS near the Fermi energy calculated for $Ca_{2.5}La_{0.5}Rh_4Sn_{13}$ at the pressure 0 and 2.1 GPa.

in [12], therefore are not shown here. All spectra measured for both series are very similar and dominated by Rh 4*d* electron states, which are located in the XPS bands between the Fermi energy ϵ_F and ~4 eV, and by Sn 5*s* states with the broad maximum centered at ~7 eV. With increasing concentration of La or Ce, the shape of the VB XPS spectra are almost the same, excluding the narrow energy range near ϵ_F, which strongly relates to the electric transport properties of these alloys. Recently, we have demonstrated that, for metallic state of the $Ca_{3-x}Ce_xRh_4Sn_{13}$ alloys, the subtle change of DOS at ϵ_F correlates well with the observed resistivity behavior $\frac{d\rho}{dP}$ giving $\frac{dN(\epsilon_F)}{dP} \propto \frac{d\rho}{dP}$ [12]. A similar effect was observed for $Ca_3Rh_4Sn_{13}$ with Ca atoms partially replaced by La. Figure A2 demonstrates the change of calculated DOS at $P = 0$ and 2.1 GPa for $Ca_{2.5}La_{0.5}Rh_4Sn_{13}$. Calculations documented the increase of the total DOS at ϵ_F with P, giving $\frac{dN(\epsilon_F)}{dP} \simeq 0.5\ eV^{-1}\ GPa^{-1}$, which correlates well with the observed negative $\frac{d\rho}{dP}$ in normal metallic state at $T = 8$ K, as shown in figure 3. This simple explanation assumes the relation $\rho \sim 1/n$ between the resistivity and the number of carriers n, that naively reflects the DOS at ϵ_F. Figure A2 also shows the energy shift of the DOS maxima with P in the vicinity of ϵ_F to higher binding

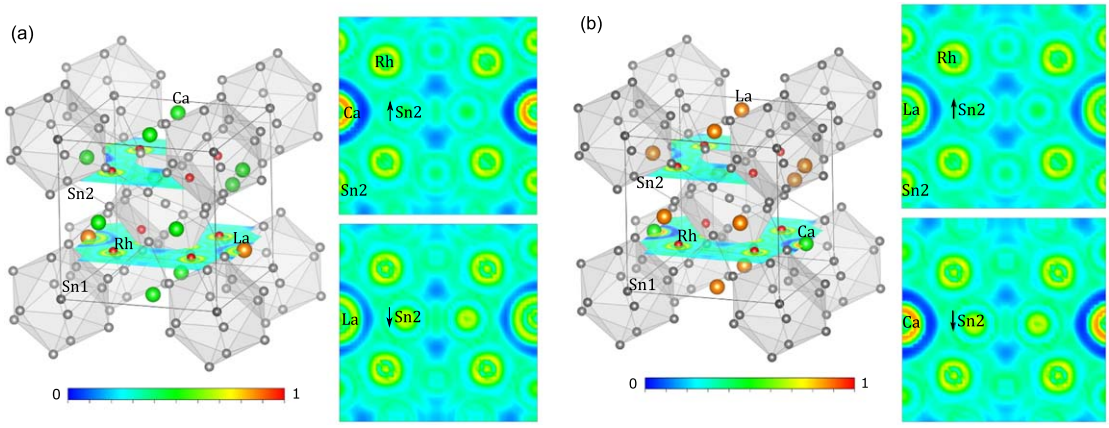

Figure A3. (a) The ELF distribution for $Ca_{2.5}La_{0.5}Rh_4Sn_{13}$ in the plane $z = \frac{3}{4}$ shown in the upper panel and in the plane $z = \frac{1}{4}$ (in lower panel). An arrow oriented up/down indicates Sn2 atom located above or below the plane. (b) The same for $Ca_{0.5}La_{2.5}Rh_4Sn_{13}$.

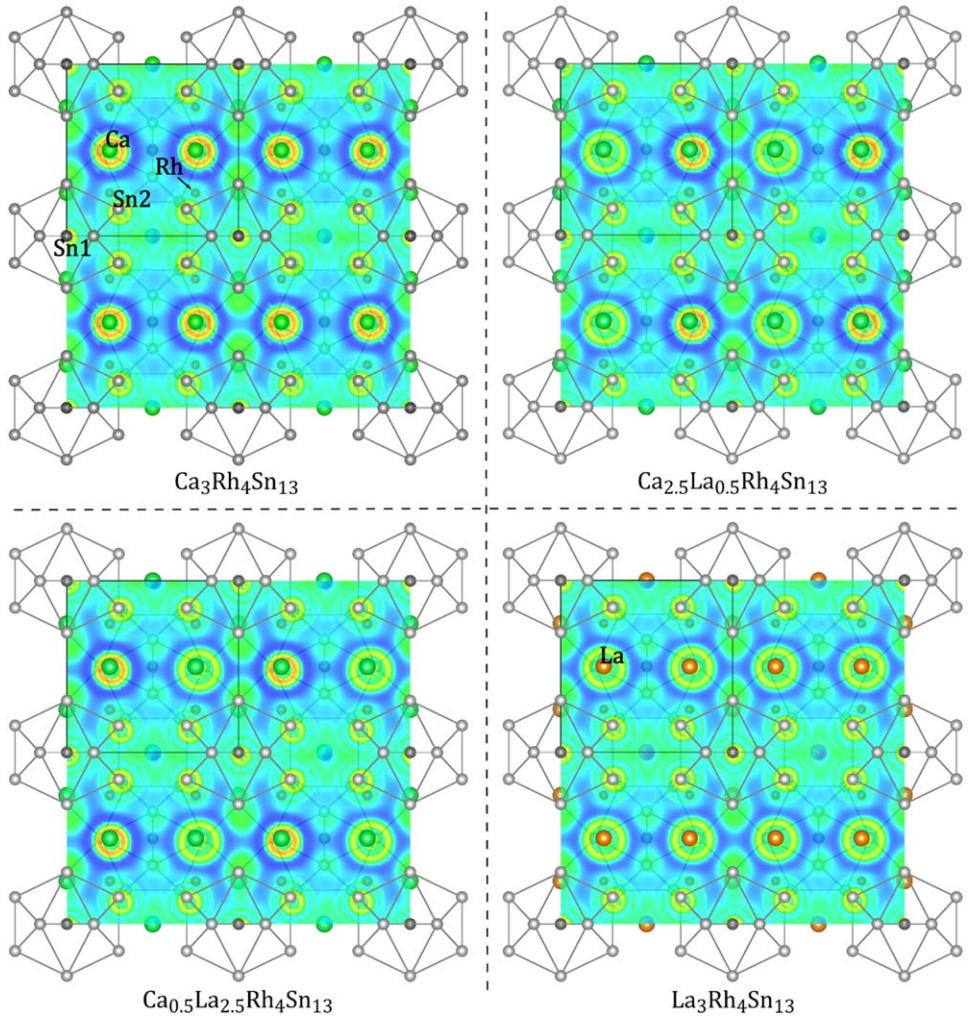

Figure A4. The ELF distribution in the plane $z = 1$ shown for series of compounds.

energy $|E|$ in respect to ϵ_F. This response for heavy Fermi metals to the applied pressure is characteristic of electron-type conductivity at high pressure [71].

Figure 3(b) exhibits at $T > T_c$ positive effect of $\frac{d\rho}{dP}$ for $Ca_{0.5}La_{2.5}Rh_4Sn_{13}$ samples rich in La. This $\frac{d\rho}{dP} > 0$ behavior, different with that observed for La-diluted $Ca_3Rh_4Sn_{13}$ alloys, was recently discussed as a result of

interband distance (pseudogap) located at the Fermi level, which increases with pressure (for details see [72]), and leads to increase in ρ under pressure.

A.1. Bonding properties investigated by ELF

For the skutterudite-related Ce $_3M_4Sn_{13}$ and La $_3M_4Sn_{13}$ compounds, where M is a d-electron metal, the charge density analysis revealed a strong charge accumulation between Sn1 atom and Sn2 atoms of the $Sn2_{12}$ cage, and between metal M or rare earth element and Sn2 atoms, which implies a strong covalent bonding interaction and leads to a subtle structural transition [2, 72, 73]. The structural deformation observed in this class of materials at $T^\star \sim 170$ K, is usually accompanied by formation of a CDW phase transition, and under external pressure $T^\star \longrightarrow 0$ defines a novel structural QCP [3]. Based on the present structural data, which documented the second order structural phase transition at a much higher temperature of about 310 K, we revise the previous understanding of the nature of $T^\star \sim 170$ K. The structural deformation, however, has not been documented for $Ca_3Rh_4Sn_{13}$. To determine the subtle bonding properties of the charge distribution in La substituted $Ca_3Rh_4Sn_{13}$ a full-potential chemical-bonding analysis via calculation of the ELF is presented within the density functional theory [74] [similar band structure ELF calculations were recently reported in [12] for cerium doped ($Ca_{1-x}Ce_xRh_4Sn_{13}$) compounds]. Figure A3 exhibit the ELF distribution in planes $z = \frac{3}{4}$ and $z = \frac{1}{4}$ for $Ca_{2.5}La_{0.5}Rh_4Sn_{13}$ and $Ca_{0.5}La_{2.5}Rh_4Sn_{13}$, respectively, while figure A4 compares the ELF isosurfaces $z = 1$ sections for parent and doped compounds. The ELF maxima are essentially located on the atoms in the plane, the charge density analysis also reveals the covalent bonding between the nearest-bounding atoms: Sn1–Sn2, Rh–Sn2 and La–Sn2 due to charge accumulation between them. These bondings are the strongest between Rh–Sn2 and Sn1 and Sn2, which can be a reason for structural distortion. XRD analysis confirms the charge modulation on the Rh atoms. As a result of this charge modulation, some of the Sn2 atoms are located closer to Rh than the remaining one, which leads to distortion of the Sn2 cages. Moreover, when Ca in $Ca_3Rh_4Sn_{13}$ is fractionally replaced by larger La or Ce atom, the Sn_{12} cage can easily be deformed due to strong chemical stresses, as is shown in figure A4 (see figure 1). The superlattice transition that is connected with Sn2 cage instability is, however, not observed in $Ca_3Rh_4Sn_{13}$.

References

[1] Remeika J P *et al* 1980 *Solid State Commun.* **34** 923–6
Hodeau J L, Marezio M, Remeika J P and Chen C H 1982 *Solid State Commun.* **42** 97–102
[2] Ślebarski A, Goraus J, Witas P, Kalinowski L and Fijałkowski M 2015 *Phys. Rev.* B **91** 035101
[3] Klintberg L E, Goh S K, Alireza P L, Saines P J, Tompsett D A, Logg P W, Yang J, Chen B, Yoshimura K and Grosche F M 2012 *Phys. Rev. Lett.* **109** 237008
[4] Tompsett D A 2014 *Phys. Rev.* B **89** 075117
[5] Kuo C N, Tseng C W, Wang C M, Wang C Y, Chen Y R, Wang L M, Lin C F, Wu K K, Kuo Y K and Lue C S 2015 *Phys. Rev.* B **91** 165141
[6] Chen X *et al* 2016 *Phys. Rev.* B **93** 235121
[7] Israel C *et al* 2005 *Physica* B **359–361** 251–3
[8] Goh S K, Tompsett D A, Saines P J, Chang H C, Matsumoto T, Imai M, Yoshimura K and Grosche F M 2015 *Phys. Rev. Lett.* **114** 097002
[9] Cheung Y W *et al* 2016 *Phys. Rev.* B **93** 241112(R)
[10] Westerveld J P A, Lo Cascio D M R and Bakker H 1987 *J. Phys. F: Met. Phys.* **17** 1963–71
[11] Westerveld J P A, Lo C, H Bakker D M R, Loopstra B O and Goubitz K 1989 *J. Phys.: Condens. Matter.* **1** 5689–702
[12] Ślebarski A, Goraus J, Maśka M M, Witas P, Fijałkowski M, Wolowiec C T, Fang Y and Maple M B 2016 *Phys. Rev.* B **93** 245126
[13] Ślebarski A, Fijałkowski M, Maśka M M, Mierzejewski M, White B D and Maple M B 2014 *Phys. Rev.* B **89** 125111
[14] Maple M B, Ho P-C, Zapf V S, Frederick N A, Bauer E D, Yuhasz W M, Woodward F M and Lynn J W 2002 *J. Phys. Soc. Japan. Suppl.* **71** 23–8
[15] Vollmer R, Faißt A, Pfleiderer C, V Löhneysen H, Bauer E D, Ho P-C, Zapf V and Maple M B 2003 *Phys. Rev. Lett.* **90** 057001
[16] Seyfarth G, Brison J P, Méasson M-A, Braithwaite D, Lapertot G and Flouquet J 2006 *Phys. Rev. Lett.* **97** 236403
[17] Méasson M-A, Braithwaite D, Lapertot G, Brison J-P, Flouquet J, Bordet P, Sugawara H and Canfield P C 2008 *Phys. Rev.* B **77** 134517
[18] Bianchi A, Movshovich R, Jaime M, Thompson J D, Pagliuso P G and Sarrao J L 2001 *Phys. Rev.* B **64** 220504(R)
[19] Ślebarski A, Maśka M M, Fijałkowski M, McElroy C A and Maple M B 2015 *J. Alloys Compds.* **646** 866–72
[20] Bordet P, Cox D E, Espinosa G P, Hodeau J L and Marezio M 1991 *Solid State Commun.* **78** 359–66
[21] Peng Y *et al* 2018 *Abstract S30.000 12 in Bulletin APS, APS March Meeting 2018 (Los Angeles, California)*
[22] Benfatto L, Caprara S and Di Castro C 2000 *Eur. Phys. J.* **17** 95–102
[23] Caprara S, Di Castro C, Seibold G and Grilli M 2017 *Phys. Rev.* B **95** 224511
[24] Rodriguez-Carvajal J 1993 *Physica* B **192** 55–69
[25] Azuah R T, Kneller L R, Qiu Y, Tregenna-Piggott P L W, Brown C M, Copley J R D and Dimeo R M 2009 *J. Res. Natl Inst. Stand. Technol.* **114** 341–58
[26] Ślebarski A, White B D, Fijałkowski M, Goraus J, Hamlin J J and Maple M B 2012 *Phys. Rev.* B **86** 205113
[27] Fang Y, Yazici D, White B D and Maple M B 2015 *Phys. Rev.* B **92** 094507
[28] Koepernik K and Eschrig H 1999 *Phys. Rev.* B **59** 1743–57
Opahle I, Koepernik K and Eschrig H 1999 *Phys. Rev.* B **60** 14035–41
Koepernik K, Velicky B, Hayn R and Eschrig H 1997 *Phys. Rev.* B **55** 5717–29
Eschrig H, Koepernik K and Chaplygin I 2003 *J. Solid State Chem.* **176** 482–95
[29] Elk FP-LAPW code, version 3.1.12, http://elk.sourceforge.net/
[30] Perdew J P and Wang Y 1992 *Phys. Rev.* B **45** 13244–9

[31] Strydom A M 2007 *J. Phys.: Condens. Matter* **19** 386205
[32] Eliashberg G M 1960 *Sov. Phys.—JEPT* **11** 696–702
Eliashberg G M 1961 *Sov. Phys.—JEPT* **12** 1000–2
[33] McMillan W L 1968 *Phys. Rev.* **167** 331–44
[34] Dynes R C 1972 *Solid State Commun.* **10** 615–8
[35] Hopfield J J 1969 *Phys. Rev.* **186** 443–51
[36] Shao Y and Zhang X 2004 *J. Phys.: Condens. Matter* **16** 1103–13
[37] Schmidt V V 1977 *The Physics of Superconductors* ed P Müllerand and A V Ustinov (Berlin: Springer)
[38] Helfand E and Werthamer N R 1964 *Phys. Rev. Lett.* **13** 686–8
Helfand E and Werthamer N R 1966 *Phys. Rev.* **147** 288–94
Werthamer N R, Helfand E and Hohenberg P C 1966 *Phys. Rev.* **147** 295–302
[39] de Gennes P G 1964 *Phys. Kondens. Mater.* **3** 79–90
Maki K 1964 *Physics* **1** 21–30
DeGennes P G 1966 *Superconductivity in Metals and Alloys* (New York: Benjamin)
[40] Usadel K D 1966 *Phys. Rev. Lett.* **25** 507–9
[41] Koshelev A E and Golubov A A 2003 *Phys. Rev. Lett.* **90** 177002
[42] Gurevich A 2003 *Phys. Rev.* B **67** 184515
[43] Geshkenbein V B, Ioffe L B and Millis A J 1998 *Phys. Rev. Lett.* **80** 5778–81
[44] de Lima O F, Awana V P S, Ribeiro R A and Avila M A 2001 *J. Magn. Magn. Mater.* **226–230** 367–9
[45] Wan-Li Y, Hai-Hu W, Yong-Ming N and Zhong-Xian Z 1999 *Acta Phys. Sin.* **8** 702–10
[46] Caixeiro E S, González J L and de Mello E V L 2004 *Phys. Rev.* B **69** 024521
[47] Méasson M-A, Braithwaite D, Lapertot G, Brison J-P, Flouquet J, Bordet P, Sugawara H and Canfield P C 2008 *Phys. Rev.* B **77** 134517
[48] Ovchinnikov Yu N and Kresin V Z 1995 *Phys. Rev.* B **52** 3075–8
[49] Ovchinnikov Y N and Kresin V Z 1996 *Phys. Rev.* B **54** 1251–63
[50] Jung S-G, Shin S, Jang H, Mikheenko P, Johansen T H and Park T 2017 *Supercond. Sci. Technol.* **30** 085009
[51] Gantmakher V F, Klinkova L A, Barkovskii N V, Tsydynzhapov G E, Wiegers S and Geim A K 1996 *Phys. Rev.* B **54** 6133–6
[52] Rasolt M and Tešanovoć Z 1992 *Rev. Mod. Phys.* **64** 709–54
Domański T, Maśka M M and Mierzejewski M 2003 *Phys. Rev.* B **67** 134507
Maśka M M 2002 *Phys. Rev.* B **66** 054533
[53] Mierzejewski M and Maśka M M 2002 *Phys. Rev.* B **66** 214527
[54] Maśka M M and Mierzejewski M 2001 *Phys. Rev.* B **64** 064501
Mierzejewski M and Maśka M M 1999 *Phys. Rev.* B **60** 6300–3
[55] Mydosh J A 1993 *Spin Glasses: An Experimental Introduction* (London: Taylor and Francis)
[56] Andersen B M, Melikyan A, Nunner T S and Hirschfeld P J 2006 *Phys. Rev.* B **74** 060501(R)
[57] Larkin A I, Mel'nikow V I and Khmel'nitskii D E 1971 *Sov. Phys.—JETP* **33** 458–62
[58] Galitski V M and Larkin A I 2002 *Phys. Rev.* B **66** 064526
[59] Mazzone D G *et al* 2015 *Phys. Rev.* B **92** 024101
[60] Kuo C N, Chen W T, Tseng C W, Hsu C J, Huang R Y, Chou F C, Kuo Y K and Lue C S 2018 *Phys. Rev.* B **97** 094101
[61] Ban W J, Wang H P, Tseng C W, Kuo C N, Lue C S and Wang N L 2017 *Sci. China-Phys. Mech. Astron.* **60** 047011
[62] Fang A F, Wang X B, Zheng P and Wang N L 2014 *Phys. Rev.* B **90** 035115
[63] Oswald I W H, Rai B K, McCandless G T, Morosan E and Chan J Y 2017 *CrystEngComm* **19** 3381–91
[64] Otomo Y, Iwasa K, Suyama K, Tomiyasu K, Sagayama H, Sagayama R, Nakao H, Kumai R and Murakami Y 2016 *Phys. Rev.* B **94** 075109
[65] Lue C S, Kuo C N, Tseng C W, Wu K K, Liang Y-H, Du C-H and Kuo Y K 2016 *Phys. Rev.* B **93** 245119
[66] Hu Y J, Cheung Y W, Yu W C, Imai M, Kanagawa H, Murakawa J, Yoshimura K and Goh S K 2017 *Phys. Rev.* B **95** 155142
[67] Bardeen J, Cooper L N and Schrieffer J R 1957 *Phys. Rev.* **108** 1175–204
[68] Seiden P E 1969 *Phys. Rev.* **179** 458–62
[69] Bochenek L, Wawryk R, Henkie Z and Cichorek T 2012 *Phys. Rev.* B **86** 060511(R)
[70] Juraszek J, Henkie Z and Cichorek T 2016 *Acta Phys. Pol.* A **130** 597–9
[71] Hai L, Zhengzhong L, Mingwen X and Xiaohua X 1999 *Commun. Theor. Phys.* **31** 49–56
Shang S 2002 *Phys. Rev.* B **65** 064407
[72] Ślebarski A, Goraus J and Witas P 2015 *Phys. Rev.* B **92** 155136
[73] Ślebarski A, Witas P, Goraus J, Kalinowski L and Fijałkowski M 2014 *Phys. Rev.* B **90** 075123
[74] Hohenberg P and Kohn W 1964 *Phys. Rev.* **136** B864–71